Article

First-Principles Calculations of Thermoelectric Transport Properties of Quaternary and Ternary Bulk Chalcogenide Crystals

Sahib Hasan [1,2], **Saro San** [1], **Khagendra Baral** [1], **Neng Li** [3], **Paul Rulis** [1] **and Wai-Yim Ching** [1,*]

[1] Department of Physics and Astronomy, University of Missouri-Kansas City, Kansas City, MO 64110, USA; sahmvd@mail.umkc.edu (S.H.); ssawcc@mail.umkc.edu (S.S.); kbx67@mail.umkc.edu (K.B.); rulisp@umkc.edu (P.R.)

[2] Department of Sciences, College of Basic Education, Al Muthanna University, Samawah 66001, Iraq

[3] School of Materials Science and Engineering, Wuhan University of Technology, No. 122, Luoshi Road, Wuhan 430070, China; lineng@whut.edu.cn

[*] Correspondence: chingw@umkc.edu

Abstract: Chalcogenide crystals have a wide range of applications, especially as thermoelectric materials for energy conversion. Thermoelectric materials can be used to generate an electric current from a temperature gradient based on the Seebeck effect and based on the Peltier effect, and they can be used in cooling applications. Using first-principles calculations and semiclassical Boltzmann theory, we have computed the Seebeck coefficient, electrical conductivity, electronic thermal conductivity, power factor, and figure of merit of 30 chalcogenide crystals. A Quantum Espresso package is used to calculate the electronic properties and locate the Fermi level. The transport properties are then calculated using the BoltzTraP code. The 30 crystals are divided into two groups. The first group has four crystals with quaternary composition (A_2BCQ_4) (A = Tl; B = Cd, Hg; C = Si, Ge, Sn; Q = S, Se, Te). The second group contains 26 crystals with the ternary composition ($A'B'Q_2$) (A' = Ag, Cu, Au, Na; B' = B, Al, Ga, In; Q = S, Se, Te). Among these 30 chalcogenide crystals, the results for 11 crystals: $Tl_2CdGeSe_4$, $Tl_2CdSnSe_4$, $Tl_2HgSiSe_4$, Tl_2HgSnS_4, $AuBSe_2$, $AuBTe_2$, $AuAlTe_2$, $AuGaTe_2$, $AuInTe_2$, $AgAlSe_2$, and $AgAlTe_2$ are revealed for the first time. In addition, temperature-dependent transport properties of pure and doped $AgSbSe_2$ and $AgSbTe_2$ crystals with dopant compositions of $AgSb_{0.94}Cd_{0.06}Te_2$ and $AgSbTe_{1.85}Se_{0.15}$ were explored. These results provide an excellent database for bulk chalcogenides crucial for a wide range of potential applications in renewable energy fields.

Keywords: chalcogenide crystals; Boltzmann theory; Seebeck coefficient; thermoelectric properties; total bond order density; density functional theory

1. Introduction

In recent years, searching for new alternative renewable energy resources has become an essential endeavor due to severe environmental concerns and the concomitant need to reduce the use of fossil fuels [1–3]. This is especially true for materials that can convert energy that would otherwise go to waste into useful work. The direct conversion between heat and electricity is crucial for many applications in power generation [4–7]. In this regard, thermoelectric (TE) materials have attracted a great deal of attention because of their ability to convert the waste heat from industrial processes into usable electricity [8]. The TE effect was first noticed by Seebeck in 1821 and was coined as the Peltier effect when used to create a temperature gradient from a supplied current [9]. This method of energy generation was used in spacecraft beginning in the early 1960s [10,11]. Since then, exploring high-efficiency thermoelectric materials for clean and renewable energy production has become one of the top priorities in materials research and development. Even though many TE devices have low efficiency, they still have been widely used in

many applications for energy harvesting. They are expected to have broad and diverse applications to the recovery of waste heat for useful work, as illustrated, for example, by the wristwatch design of the Seiko and Citizen companies [12,13].

The overall performance of a TE material is measured by a dimensionless figure of merit parameter ZT, given by $ZT = S^2 \sigma T / (\kappa_{lat} + \kappa_{ele})$, where S, σ, T, κ_{lat}, and κ_{ele} are the Seebeck coefficient, electrical conductivity, absolute temperature, lattice thermal conductivity, and electronic thermal conductivity, respectively. σ is given by $\sigma = nem$, where n is the carrier concentration, e is the electron charge, and m is the electron mobility. The σ and κ_{ele} are related by $\kappa_{ele} = L_0 \sigma T$, where L_0 is the Lorenz number [14]. $S^2 \sigma$ is called power factor (PF). For excellent TE materials, ZT should be larger than unity [15,16]. Many efforts have been dedicated to increase ZT by new innovative approaches such as using nanowires, nano-structured materials, band structure engineering, lattice anharmonicity, and two-dimensional materials technology [17–22].

Various materials are used for thermoelectricity over a wide range of temperatures, including polymeric and inorganic materials. However, inorganic semiconductors have been found to be the most efficient [23,24]. Among the inorganic materials, chalcogenide compounds have attracted a great deal of attention. They generally have high electrical conductivity and low thermal conductivity resulting in higher ZT values [25]. Chalcogenide compounds contain at least one of the chalcogen elements (S, Se, Te) and one or more electropositive, in a few cases, electronegative elements. The electropositive elements are mostly from group IB (Cu, Ag), IIB (Zn, Cd, Hg), IVA (Si, Ge, Sn), IIIA (In, Tl), IVB (Zr, Hf), IIA (Mg, Ba), and IA (Li, K, Cs) in the periodic table. In some cases, lanthanide elements such as La and Lu can also be involved. This diverse compositional space makes chalcogenide compounds a unique class of materials rarely seen in other materials such as semiconductors, large gap insulators, superconductors, silicates glasses, metallic alloys, etc. Many quaternary chalcogenide crystals, such as A^I–B^{III}–C^{IV}–X^{VI} system (A^I = Cu, Ag; B^{III} = Ga, In; C^{IV} = Si, Ge, Sn; X^{VI} = S, Se, Te), and $A^I_2 B^{II} C^{IV} Q_4$ system (A^I = Cu, Ag; B^{II} = Mg, Mn, Fe, Zn, Cd, and Hg; C^{IV} = Si, Ge, Sn; and Q = S, Se, Te) are very popular due to their compositional flexibility and functional turnability ideal for TE applications [26–30]. They are also extensively used in optical [31] and nonlinear optical devices in the visible-infrared region, photovoltaic cells [32–38], solar energy converters [39–42], and magnetic applications [43]. Another group of chalcogenide crystals in the form of $Ag_2 XYQ_4$ (X = Ba, Sr; Y = Ge, Sn; Q = S, Se) are also very attractive [44].

Several experimental and theoretical pieces of research have been carried out recently to enhance the thermoelectric performance and increase the ZT of some chalcogenide crystals. C. Wang et al. [45] has succeeded recently in achieving ZT higher than one for Ag-doped crystalline $CuInTe_2$, where ZT was increased for $Cu_{1-x} Ag_x InTe_2$ from 0.6 (at x = 0) to 1.4 (at x = 0.25). A very high enhanced figure of merit ($ZT \approx 2.6$ at 573 K) was obtained in Cd-doped polycrystalline $AgSbTe_2$ [46]. Another study [47] showed that ZT increased to maximum value ($ZT \approx 1.35$ at 600 K) for $AgSbTe_{2-x} Se_x$ (at x = 0.02). S. Deng et al. [48] showed that the TE performance could be enhanced for Ga-doped $CuInTe_2$ crystal ($CuIn_{1-x} Ga_x Te_2$), and ZT can be increased to the maximum value ($ZT = 0.8$ at 773 K) for the $CuIn_{0.8} Ga_{0.2} Te_2$ sample due to the lower thermal conductivity. Y. Zhong et al. [49] found that Ag vacancy and In dopant substitution in the $AgGaTe_2$ system can lower the lattice thermal conductivity (κ_{lat}) significantly, which can produce a higher value of ZT ($ZT \approx 1.44$).

SnTe is another type of chalcogenide crystal that has been under extensive experimental and theoretical studies for a long time. Recently, A. Rifqi et al. [50] succeeded in enhancing the TE performance of Ti-doped SnTe crystal ($Sn_{1-x} Ti_x Te$) and Zr-doped SnTe crystal ($Sn_{1-x} Zr_x Te$). They increased ZT from 0.41 to 0.51 at 700 K for $Sn_{0.97} Ti_{0.03} Te$ (x = 0.03), and from 0.45 to 0.55 at 700 K for $Sn_{0.98} Zr_{0.02} Te$ (x = 0.02). New experimental techniques have been used recently to achieve higher ZT for some chalcogenides. For example, by using new mechanical alloying combined with microwave-assisted synthesis for the synthesis of single-phase cubic isocubanite $CuFe_2 S_3$, a maximum thermoelectric figure

of merit, $ZT_{\max} \approx 0.14$ at 673 K, was achieved for $CuFe_2S_3$ crystal [51]. Thermoelectric transport properties of another important group of chalcogenides, Tl_2PbXY_4 (X = Zr, Hf and Y = S, Se), have been reported recently by S. Azam et al. [52]. According to this study, these four crystals possess high TE performance and high ZT (ZT = 0.85, 0.71, 0.725, and 0.68 at 800 K for Tl_2PbHfS_4, $Tl_2PbHfSe_4$, Tl_2PbZrS_4, and $Tl_2PbZrSe_4$ crystals respectively).

The crystal structure, electronic structure, and the optical properties of quaternary chalcogenides $Tl_2B^{II}C^{IV}Q_4$ (B^{II} = Cd, Hg; C^{IV} = Si, Ge, Sn; Q = S, Se, Te) have been reported recently [53–56]. They are semiconductors with potential TE applications but have not yet been sufficiently explored so far. Bagci et al. [57] reported the chemical-potential-dependent transport properties of the chalcopyrite crystals $CuBQ_2$ (Q = S, Se, Te). However, they did not include the temperature dependency of the transport properties. Although the TE properties of ADQ_2 (A = Cu, Ag; D = Ga, In; Q = Se, Te) chalcopyrite were studied extensively [58–64], much less research has been conducted on $AuBQ_2$ and $AgAlQ_2$ (Q = S, Se, Te). On the other hand, the electronic structure and optical properties of $AuBQ_2$ and $AgAlQ_2$ were reported recently [65,66] without the TE transport properties. The TE properties of the ternary chalcogenide crystals $AgSbSe_2$ and $AgSbTe_2$ were studied sixty years ago in the 1950s [67]. These two crystals belong to the I-V-VI$_2$ family, where I = Cu or Ag, V = Sb or Bi, and VI = S, Se, and Te. They were considered promising p-type TE materials because of their low thermal conductivity [68–70]. Both of these crystals can crystallize in a rock salt crystal structure (space group 225, $Fm\bar{3}m$) with disordered Ag and Sb atoms [71]. Another study [72] revealed that they are semiconductors with a very narrow energy band gap ($E_g \approx 0.03$ eV) or that they are semi-metallic. TE performance for $AgSbSe_2$ and $AgSbTe_2$ can be significantly enhanced (e.g., ZT is greater than 1) when properly doped by Pb, Bi, Cd, Sn, Se, or Ce dopants [46,47,73–76].

Motivated by the realization of the unique properties of the above crystals, we investigate the TE transport properties of 30 chalcogenide crystals as listed in Table S1 in the Supplementary Information (SI) by using density functional theory and semiclassical Boltzmann theory. The results for these 30 crystals are presented in Section 3.1. These 30 crystals are divided into two main groups: crystals 1–4 with stoichiometry A_2BCQ_4 (A = Tl; B = Cd, Hg; C = Si, Ge, Sn; Q = S, Se, Te) (colored white in Table S1 and Table 1), crystals 5–30 with stoichiometry ($A'B'Q_2$) (A = Ag, Cu, Au, Na; B' = B, Al, Ga, In; Q = S, Se, Te). The crystals 5–30 are divided into six subgroups (colored gray and white in Table S1 and Table 1). In all subsequent discuss ions, the same specific order and ID number for these crystals are maintained. The fully optimized structures are listed in Table S1 with the corresponding experimental lattice parameters. Moreover, we further investigated the crystals $AgSbSe_2$, $AgSbTe_2$, Cd-doped $AgSbTe_2$ ($AgSb_{0.94}Cd_{0.06}Te_2$), and Se-doped $AgSbTe_2$ ($AgSbTe_{1.85}Se_{0.15}$) by using the same computational methods, and their results are presented in Section 3.2. Such comprehensive studies have added valuable insight into chalcogenide crystal sciences and are to provide a comprehensive review for the industry. In the following section, we briefly describe the computational methods used, followed by the results and discussions section. We end up with a brief conclusion and our vision for the future study on how to improve their thermoelectric performance.

Table 1. The highest values of ZT and the values of the carrier concentrations (*n*) at which these values of ZT occur, highest PF, and highest κ_{ele}/τ for the 30 chalcogenide crystals.

#	Crystal	n (e$^-$/cm^3)	Highest ZT	Highest PF (mW/cm.K^2)	κ_{ele} (W/m.K) at 900 K
1	$Tl_2CdGeSe_4$	10^{20}	0.966(750 K)	0.634(800 K)	0.60
2	$Tl_2CdSnSe_4$	10^{19}	0.947(750 K)	0.415(800 K)	0.408
3	$Tl_2HgSiSe_4$	-10^{20}	0.915(550 K)	0.945(800 K)	0.934
4	Tl_2HgSnS_4	$10^{20}, -10^{20}$	0.943(900 K), 0.853(900 K)	1.49(850 K), 1.12(900 K)	0.199, 1.18
5	$CuBS_2$	10^{20}	0.933(900 K)	1.88(750 K)	1.77

Table 1. *Cont.*

#	Crystal	n (e$^-$/cm^3)	Highest ZT	Highest PF (mW/cm.K^2)	κ_{ele} (W/m.K) at 900 K
6	CuBSe$_2$	-10^{19}	0.882(900 K)	2.29(900 K)	2.34
7	CuBTe$_2$	10^{19}	0.951(900 K)	1.57(850 K)	1.48
8	AuBSe$_2$	10^{20}, 10^{19}	0.873(800 K), 0.889(650 K)	3.72(800 K), 1.57(650 K)	3.86, 1.7
9	AuBTe$_2$	10^{20}	0.802(900 K)	3.42(900 K)	3.84
10	AuAlTe$_2$	10^{20}	0.778(750 K)	2.35(750 K)	2.27
11	AuGaTe$_2$	-10^{20}, 10^{20}	0.495(700 K), 0.55(400 K)	3.85(700 K), 1.58(400 K),	7.83, 5.87
12	AuInTe$_2$	-10^{19}, 10^{20}	0.431(800 K), 0.536(400 K)	3.25(800 K)	7.57
13	CuAlSe$_2$	10^{18}, 10^{19}, 10^{20}	0.944(750 K), 0.935(850 K), 0.888(900 K)	0.38(750 K), 0.68(850 K), 2.15(900 K)	0.353, 0.647, 2.18
14	CuAlTe$_2$	-10^{18}, 10^{18}	0.952(800 K), 0.947(850 K),	0.403(800 K), 0.577(850 K)	0.381, 0.549
15	AgAlSe$_2$	-10^{19}, -10^{18}, 10^{18}	0.960(900 K), 0.956(900 K), 0.955(900 K)	0.548(900 K), 0.748(900 K), 0.788(900 K)	0.514, 0.705, 0.743
16	AgAlTe$_2$	10^{20}, 10^{19}	0.858(900 K), 0.977(250 K)	2.04(900 K)	2.14
17	CuGaS$_2$	10^{21}, 10^{20}	0.607(900 K), 0.910(500 K)	5.48(900 K), 0.475(500 K)	8.13, 0.855
18	CuGaSe$_2$	10^{20}, -10^{19}	0.688(600 K), 0.784(350 K)	2.26(600 K), 0.831(350 K)	3.77, 2.24
19	CuGaTe$_2$	10^{20}, -10^{18}, 10^{19}	0.739(700 K), 0.885(300 K), 0.847(400 K)	3.41(700 K), 0.352(300 K), 1.02(400 K)	4.96, 2.96, 3.04
20	AgGaS$_2$	-10^{20}, -10^{19}	0.865(900 K), 0.823(900 K)	2.03(900 K), 2.81(900 K)	2.11, 3.07
21	AgGaSe$_2$	10^{20}	0.735(650 K)	1.86(650 K)	2.79
22	AgGaTe$_2$	10^{20}, 10^{19}	0.729(800 K), 0.824(400 K)	2.86(900 K), 0.803(400 K)	3.76, 1.76
23	CuInS$_2$	10^{21}, 10^{20}	0.633(900 K), 0.810(350 K)	5.03(900 K), 1.21(350 K)	7.16, 2.73
24	CuInSe$_2$	10^{21}	0.541(900 K)	4.67(900 K)	7.78
25	CuInTe$_2$	10^{20}	0.79(at 500 K)	1.85(500 K)	3.24
26	AgInS$_2$	10^{20}, 10^{18}, -10^{18}	0.824(750 K), 0.945(300 K), 0.986(250 K)	1.91(750 K), 0.151(300 K)	2.19, 0.75, 0.76
27	AgInSe$_2$	10^{20}	0.736(450 K)	1.31(450 K)	2.54
28	AgInTe$_2$	10^{20}	0.794(600 K)	1.97(600 K)	2.81
29	NaInSe$_2$	-10^{19}, -10^{18}, 10^{18}, 10^{19}	0.956(900 K), 0.948(900 K), 0.946(900 K), 0.94(900 K)	0.308(900 K), 0.433(900 K), 0.457(900 K), 0.557(900 K)	0.29, 0.411, 0.435, 0.533
30	NaInTe$_2$	10^{20}	0.952(850 K)	0.335(850 K)	0.565

2. Computational Methods

In this work, two well-defined density functional theory (DFT) based methods were used for specific targeted goals, which are: (1) the Orthogonalized Linear Combination of Atomic Orbitals (OLCAO) method [77] and (2) Quantum Espresso (QE) [78]. All the calculations have been performed based on the previously studied crystals [79,80], relaxed by Vienna Ab initio Simulation Package (VASP) [81]. The Spin–Orbit Coupling (SOC) effect was not included in our DFT calculations. The OLCAO method was used to calculate the electronic structure and the interatomic bonding [77]. OLCAO is an all-electron method based on the local density approximation. It uses the atomic orbitals that are themselves expanded as Gaussian-type orbitals (GTO) on the basis of expansion of the solid-state wave function. The use of localized atomic orbitals in the basis expansion, in contrast to the plane-wave expansion, is particularly effective for both crystalline [79,82–85] and non-crystalline materials [86–88], especially those with complex structures typical in the biomolecular systems [89,90]. A sufficiently large number of k-points ($10 \times 10 \times 12$ for the crystals 1–4, to $16 \times 16 \times 8$ for most crystals 5–30) were used for band structure calculations based on the size of the crystal. We used the Mulliken scheme [91] for the calculation of partial charge (PC) and interatomic bonding. The PC of an atom is defined as the charge deviation of the effective charge Q* from the charge of neutral atom (Q$_0$) in units of electron charge. Mathematically, $\Delta Q = Q_0 - Q*$. Negative ΔQ implies a gain of electrons (i.e., an electronegative ion), and positive ΔQ implies a loss of electrons (i.e., electropositivity).

Equations (1) and (2) show the formulae for effective charge (Q_α^*) and bond order (BO) values, also called the overlap population, $\rho_{\alpha\beta}$ between any pair of atoms (α, β).

$$Q_\alpha^* = \sum_i \sum_{m,occ} \sum_{j,\beta} C_{i\alpha}^{*m} C_{j\beta}^m S_{i\alpha,j\beta} \tag{1}$$

$$\rho_{\alpha\beta} = \sum_{m,\,occ} \sum_{i,j} C_{i\alpha}^{*m} C_{j\beta}^m S_{i\alpha,j\beta} \tag{2}$$

In the above equations, $S_{i\alpha,j\beta}$ are the overlap integrals between the ith orbital in the αth atom and the jth orbital in βth atom. $C_{j\beta}^m$ is the eigenvector coefficients of the mth occupied band. The BO (Equation (2)) defines the relative strength of the bond. The summation of all BO values in the crystal gives the total bond order (TBO). We obtain the total bond order density (TBOD) when TBO is normalized by the cell volume. TBOD is a single quantum mechanical metric to describe the internal cohesion of the crystal [92].

For the thermoelectric transport properties, Quantum Espresso (QE) was used to calculate the total energy, band structure, Fermi level energy, etc. The generalized gradient approximation (GGA) of Perdew, Burke, and Ernzerhof (PBE) potential was used in QE [78,93]. QE uses plane waves as basis set that includes the scalar relativistic effects in the pseudo-potentials. In this study, the energy cut-off of the plane waves was set to be 40 Ryd ($\approx$544 eV). In the QE calculations for the electronic and band structure for transport properties using BoltzTraP code, we needed denser k-point meshes for self-consistent calculations. Therefore, after careful convergence tests, a grid of $12 \times 12 \times 16$ k-points was used for the crystals 1–4, while a grid of $18 \times 18 \times 9$ k-points was found to be sufficient in most crystals 5–30 for the self-consistent calculations. The AgSbSe$_2$ and AgSbTe$_2$ crystals with 16 atoms in the unit cell have fully relaxed lattice parameters of a = 5.8010Å and 6.0991 Å, respectively. While a supercell with 64 atoms was created for both the Cd-doped AgSbTe2 (AgSb$_{0.94}$Cd$_{0.06}$Te$_2$) and Se-doped AgSbTe$_2$(AgSbTe$_{1.85}$Se$_{0.15}$) crystals, which have relaxed lattice parameters of a = 12.1977 Å and 12.2109 Å respectively. For the cubic supercell of AgSbTe$_{1.85}$Se$_{0.15}$, we started creating $2 \times 2 \times 2$ supercells from the fully relaxed cubic crystal structure of AgSbTe$_2$ with eight atoms. In the second step, five Te atoms, located at different and totally random sites of the supercell, were replaced by five Se atoms. The sites at the six faces of the supercell were avoided. The second step was followed by fully VASP relaxation for the supercell. Another last VASP relaxation step was performed to make sure that each atom took its normal position (that minimizes the energy) in the supercell.

A special feature in QE is the ability to calculate TE transport properties using the semiclassical Boltzmann theory within the constant scattering time approximation (CSTA) as implemented in the BoltzTraP code [94]. In this theory, the Seebeck coefficient, electrical conductivity, and electronic thermal conductivity can be expressed in the following equations [94]:

$$S_{\alpha\beta}(T,\ \mu) = \frac{1}{eT\Omega\sigma_{\alpha\beta}(T,\ \mu)} \int \sigma_{\alpha\beta}(\varepsilon)(\varepsilon - \mu)\left[-\frac{\delta f_0(T,\ \varepsilon,\ \mu)}{\delta\varepsilon}\right] d\varepsilon \tag{3}$$

$$\sigma_{\alpha\beta}(T,\ \mu) = \frac{1}{\Omega} \int \sigma_{\alpha\beta}(\varepsilon)\left[-\frac{\delta f_0(T,\ \varepsilon,\ \mu)}{\delta\varepsilon}\right] d\varepsilon \tag{4}$$

$$\kappa_{\alpha\beta}(T,\ \mu) = \frac{1}{e^2 T\Omega} \int \sigma_{\alpha\beta}(\varepsilon)(\varepsilon - \mu)^2 \left[-\frac{\delta f_0(T,\ \varepsilon,\ \mu)}{\delta\varepsilon}\right] d\varepsilon \tag{5}$$

Here, $\sigma_{\alpha\beta}$ are the transport distribution tensor elements calculated using the Fourier interpolation of the band structure. α and β are the tensor indices; Ω, μ, f_0, and T are the cell volume, chemical potential, Fermi distribution function, and absolute temperature, respectively.

The input data needed to run BoltzTraP code are the crystal structure and the band structure on a uniform grid. The BoltzTraP code solves the Boltzmann equation [95],

$$\frac{\partial}{\partial t}f + \vec{v}\,\frac{\partial}{\partial \vec{r}}f + \frac{eE}{h}\frac{\partial}{\partial \vec{k}}f = \left(\frac{\partial f}{\partial t}\right)_{scattering} \tag{6}$$

where, f is the distribution function, v is the velocity vector of the particle, and k is the wave vector.

BoltzTraP code solves the Boltzmann equation by interpolating a band structure and performing all required integrations. The BoltzTraP code has been tested over the last decade on different materials ranging from superconductors [96] to thermoelectric materials [97–100]. Good agreement with the experimental values was achieved in many cases [101–103]. It should be pointed out that the *ZT* values obtained here are slightly overestimated because the phonon contribution to the thermal conductivity was ignored due to the limitation of the BoltzTraP code. The BoltzTraP code treats the lattice thermal conductivity contributed by phonons as a constant and provides only the electronic part of the thermal conductivity. Several simplifying approximations are introduced. The chemical potential (μ) is set to the Fermi level energy (μ_F) because conductivities (thermal and electronic) depend proportionally on the relaxation time τ within the constant relaxation time framework. Those values can then simply be multiplied by the constant relaxation time (10^{-14} s, as this value is used in BoltzTraP code) to obtain the final transport properties. The Seebeck coefficient does not depend on the relaxation time within the constant relaxation time approximation. The CSTA assumes that the relaxation time τ is independent of energy. Hence the power factor is τ dependent, and *ZT* is τ independent. Nevertheless, this method has successfully described the transport properties of a wide range of thermoelectric materials [94,104–106].

3. Results and Discussion

3.1. Transport Properties of 30 Chalcogenide Crystals

The DFT calculations for the energy band gap (E_g) for some of these 30 crystals were published in our two previous works [79,80], and we have listed them in the third column of Table S2. In this work, we mostly focus on the crystals of the first group (the crystals: 1–4), and the crystals of the first (the crystals: 5–7), second (the crystals: 8–12), and third (the crystals: 13–16) subgroups of the second group (total crystals: 1–16), for which the transport properties are calculated for the first time. The calculated *S* and PF with varying ranges of μ for these 16 crystals at three different temperatures (300 K, 500 K, and 800 K) are shown in Figures S1 and S2 in the SI. Figures S3 and S4 show the *S* and PF versus the chemical potential for the remaining 14 crystals in the second main group. Figures S5–S7 show the electrical conductivity, electronic thermal conductivity, and the figure of merit versus the chemical potential for all 30 crystals. It is crucial to point out that all chemical-potential-dependent transport properties (including *ZT* in Figure 1) at three fixed temperatures (300 K, 500 K, and 800 K) were calculated by fixing the temperature and letting the carrier concentrations change. That means for a fixed temperature, the chemical potential is simply a function of carrier concentration, and the chemical potential μ can vary.

Table S2 shows the calculated values of *S* and *ZT* for these 30 crystals at room temperature (300 K). *S* can vary with the variation of the carrier concentration, which determines the value of the induced thermoelectric voltage due to the difference in temperature across the material. *S* is very sensitive to chemical potential, carrier concentration, and temperature. The positive value of *S* shows that holes have a dominant contribution to the conduction (p-type TE material), while the negative value of *S* shows that electrons have a dominant contribution to the conduction (n-type TE material). In insulators, *S* has the highest values around the Fermi energy, or $\mu - \mu F \approx 0$, because the carrier concentrations are at their lowest values. It is evidently observed from Figures S1 and S3 that *S* is significantly improved in the vicinity of $\mu - \mu F = 0$, which indicates that a fairly large value of *S* can be

attained by small n-type or p-type doping. From Figures S1 and S3, we can also notice that the highest S can be found in the crystals 5-CuBS$_2$, 6-CuBSe$_2$, 29-NaInSe$_2$, and 30-NaInTe$_2$ with values: 2600, 2500, 2400, and 2100 μV/K respectively for p-type crystals. Generally, the maximum value of S is obtained at room temperature, 300 K (without fixing the carrier concentrations), and S decreases with an increase in temperature at certain values of chemical potential. Much fewer previous studies for the chemical potential transport properties of these 30 crystals were found in the literature, so we are unable to compare all our results in Table S2. S values in Table S2 may coincide with high values of electronic thermal conductivity, so it is necessary to fix the carrier concentrations when calculating S as a function of temperature.
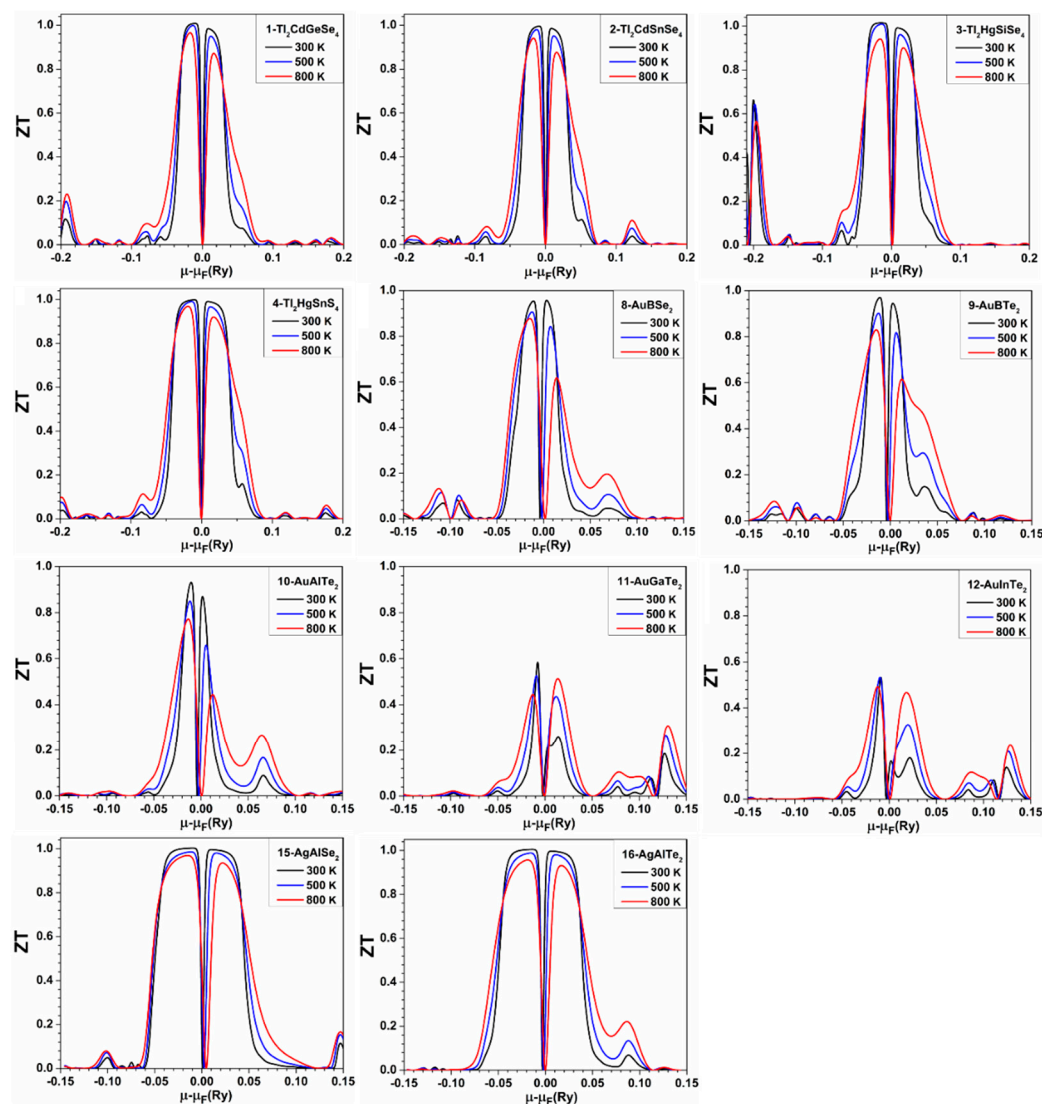
Figure 1. *ZT* versus the chemical potential for the crystals: 1-Tl$_2$CdGeSe$_4$, 2-Tl$_2$CdSnSe$_4$, 3-Tl$_2$HgSiSe$_4$, 4-Tl$_2$HgSnS$_4$, 8-AuBSe$_2$, 9-AuBTe$_2$, 10-AuAlTe$_2$, 11-AuGaTe$_2$, 12-AuInTe$_2$, 15-AgAlSe$_2$, and 16-AgAlTe$_2$.

Another important parameter that can determine the TE performance of a material is the power factor (PF). Figure S2 shows the PF as a function of the chemical potential at three different temperatures, 300 K, 500 K, and 800 K for crystals: 1–16, while the results for the remaining crystals are shown in Figure S4. As can be seen in these figures, the highest PF occurs at 800 K for all crystals, except for 29-NaInSe$_2$, for which the highest value of PF occurs at 500 K instead of 800 K. We mentioned previously that S has its maximum value at

300 K, but this is only true at Fermi level energy ($\mu - \mu_F = 0$), or around Fermi level energy ($\mu - \mu_F \approx 0$), where σ also has its minimum values (almost zero). However, S could have its maximum values at 800 K instead of 300 K when the chemical potential μ has values that are not very close to μ_F value, and this is the main reason why PF has its maximum values at 800 K for most crystals at those values of chemical potential (μ has values that are not close to μ_F). If the maximum PF occurs when $\mu - \mu_F < 0$ (hole doping region), then the implication is -that this material works better as a p-type TE material. Conversely, when $\mu - \mu_F > 0$ (electron doping region), then the crystal works better as an n-type TE material. The material should possess a high σ to present a high TE efficiency. The variation of σ with the chemical potential at three different temperatures is depicted in Figure S5. From the graph of electrical conductivity (σ/τ) in Figure S5, most crystals that have a high σ/τ in the hole doping region also have high PF values in this region compared to the electron doping region. Conversely, most crystals, which have a high σ/τ in the electron doping region, also have a high PF in this region compared to the hole doping region. The maximum σ for some crystals is observed for n-type doping, while it is observed for p-type in other crystals. One should keep in mind that these calculations were performed without fixing the carrier concentration. In order to know more about the temperature-dependent TE properties of these crystals, it is necessary to fix the carrier's concentration. Figure 1 displays the figure of merit ZT with varying ranges of μ for the crystals: 1–4, 8–12, and 15–16 at three different temperatures (300 K, 500 K, and 800 K). Figure S7 in the SI shows ZT versus the chemical potential for the remaining 19 crystals. The highest values of ZT as a function of μ for these 30 crystals are represented in the sixth column of Table S2. From Table S2, ZT for 1-$Tl_2CdGeSe_4$, 2-$Tl_2HgSiSe_4$, 5-$CuBS_2$, 6-$CuBSe_2$, 15-$AgAlSe_2$, 16-$AgAlTe_2$, 20-$AgGaS_2$, 29-$NaInSe_2$, and 30-$NaInTe_2$ is larger than unity.

The Seebeck coefficient predicted by the theory for metals and degenerate semiconductors, with a parabolic band, and the energy-independent charge carrier scattering approximation [107], depends on the carrier concentration of electrons or holes n and the effective mass m^*. It can be given by [108]:

$$S = \frac{8\pi^2 k_B^2}{3eh^2} m^* \times T \left(\frac{\pi}{3n}\right)^{2/3} \tag{7}$$

where n is the carrier concentration (electrons or holes), k_B and e are the Boltzmann constant and electronic charge, respectively. S is proportional to T, so S increases due to the increase in temperature. However, κ_{ele} will also increase with increasing temperature, leading to reduced ZT and TE performance. Decreasing ZT with increasing T may be a problem for the TE performance, but it can be solved sometimes by changing the carrier concentration, which in turn will modify the Fermi level energy, leading to increased ZT with the increase in temperature. Doping (i.e., the introduction of either additional hole or electron carriers) has an enormous effect on electronic transport properties. Doping will set the Fermi level (μ_F) and will directly influence the values of the transport properties.

In order to ensure that the Seebeck coefficient is large, there should only be a single type of carrier. Mixed n-type and p-type conduction will lead to both charge carriers moving to the cold end, canceling out the induced Seebeck voltages. Low carrier concentration insulators and even semiconductors may have large Seebeck coefficients; see Equation (6). However, low carrier concentration also results in low electrical conductivity. A compromise between large S and high electrical conductivity in thermoelectric materials must be struck to maximize the figure of merit ZT ($S^2 \sigma T/\kappa$) where κ is the thermal conductivity.

This peak typically occurs at carrier concentrations between 10^{18} and 10^{21} carriers per cm^3 (depending on the material system), which falls in between common metals and semiconductors—that is, concentrations found in heavily doped semiconductors. The next dataset describes the transport properties for both n-type and p-type systems at fixed doping levels ranging from 10^{18} to 10^{21} cm^{-3}, increasing the doping by one order of magnitude at each step.

The calculated values of S, κ_{ele}, PF, and ZT as a function of temperature at fixed values of carrier concentration in the ranges ($\pm 10^{18}$, $\pm 10^{19}$, $\pm 10^{20}$, $\pm 10^{21}$ in e^-/cm^3) for the crystals: 1–16 are shown in Figures 2–5, while the results for the remaining crystals are shown in Figures S9 and S10. A positive value of n indicates hole doping, while a negative value of n indicates electron doping. Figure 2 is for S, Figure 3 is for κ_{ele}, Figure 4 is for the PF, and Figure 5 is for ZT. The temperature range was set to be from 250 K to 900 K. Table 1 shows the highest values of ZT for these crystals, the carrier concentrations for which the highest ZT values occur, the highest PFs, and the highest κ_{ele}. In Figures 2–5 and Table 1, the value of the carrier concentration (n) for each crystal was considered to be the value that can achieve the highest ZT. It is known that a narrow band gap correlates with a large carrier concentration because many charge carriers will transfer from the valence band to the conduction band. Figure 2 shows that S increases with increasing temperature at the indicated values of n and that S has positive values indicating p-type thermoelectric materials, except for the crystals 4-Tl_2HgSnS_4, 7-$CuBTe_2$, 11-$AuGaTe_2$, and 12-$AuInTe_2$ for which S has negative values, indicating n-type TE materials. The crystal 8-$AuBSe_2$ has the highest values of S and ZT among the five crystals: 8-$AuBSe_2$, 9-$AuBTe_2$, 10-$AuAlTe_2$, 11-$AuGaTe_2$, and 12-$AuInTe_2$. As can be seen from Table 1 and Figures 2–5, for most of these crystals, the highest values of S and ZT occur with hole doping, except for the crystals 3-$Tl_2HgSiSe_4$, 6-$CuBSe_2$, 14-$CuAlTe_2$, and 20-$AgGaS_2$ where S and ZT can have the highest values with electron doping.
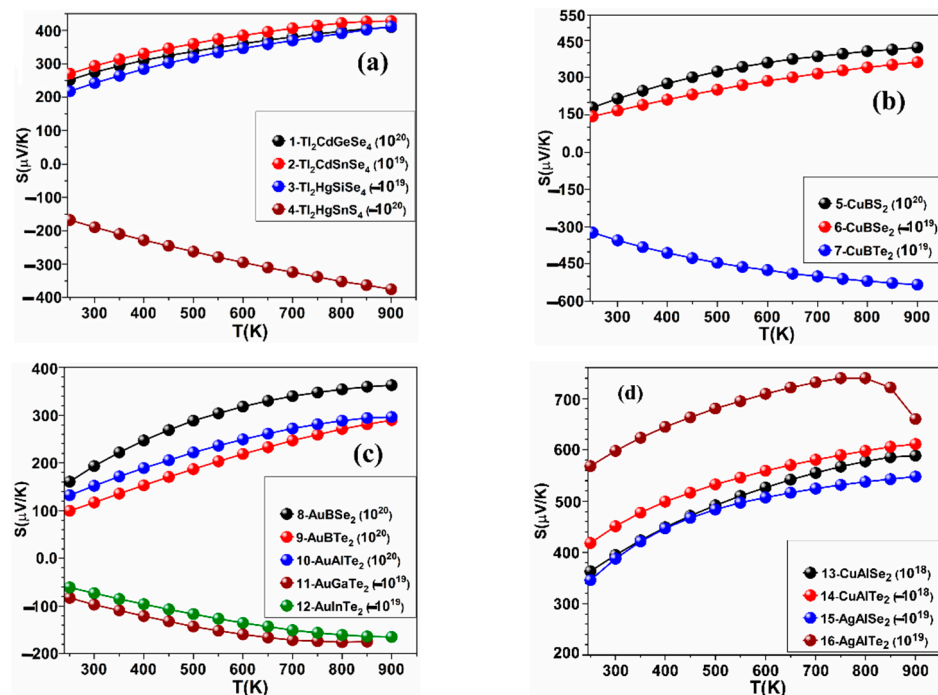
Figure 2. Calculated S versus temperature for (**a**) the crystals 1–4, (**b**) the crystals 5–7, (**c**) the crystals 8–12, and (**d**) the crystals 13–16.

The values of the electronic thermal conductivity κ_{ele}/τ and PF in Figures 3 and 4 must be multiplied by the scattering time factor, which was taken to be 10^{-14} s in our study, as mentioned in Section 2 (computational methods). From Table 1, the highest κ_{ele} occurs at 900 K for all 30 crystals. κ_{ele} has the largest value (κ_{ele} = 8.13 W/m.K) in the crystal 17-CuGaS2, while it has the smallest value (κ_{ele} = 0.199 W/m.K) in the crystal 4-Tl_2HgSnS_4. Hence, the values of κ_{ele} for all these 30 crystals are in the range from 0.199 W/m.K to 8.13 W/m.K, which indicates that the 30 crystals are very good TE materials if we know that the thermal conductivity value of the non-doped regular semiconductors such as silicon and germanium are 150 and 58 W/m.K for these two semiconductors respectively. Excellent TE materials should have a high PF (more than 3.0 mW/cm.K^2). In general, if PF is greater

than κ results in larger *ZT* and vice versa, namely 17-crystal CuGaS$_2$ and 29-NaInSe2, as shown in Table 1. Some crystals, such as 4-Tl$_2$HgSnS$_2$, 18-CuGaSe$_2$, 19-CuGaTe$_2$, and 29-NaInSe$_2$, can have a high value of *ZT* at both regions (hole and electron doping). From Table 1, we notice an interesting fact about crystals: 18-CuGaSe$_2$ and 23-CuInS$_2$ can have a high value of *ZT* (0.784 and 0.81 respectively) at a low temperature (350 K) at the following values of *n*: -10^{19} and 10^{20} e$^-$/cm^3 respectively. Additionally, the crystals 19-CuGaTe$_2$ and 26-AgInS$_2$ can have high *ZT* (0.885 and 0.945, respectively) at 300 K at the values of *n*: -10^{18} and 10^{18} e$^-$/cm^3, respectively, and these are new and interesting findings.
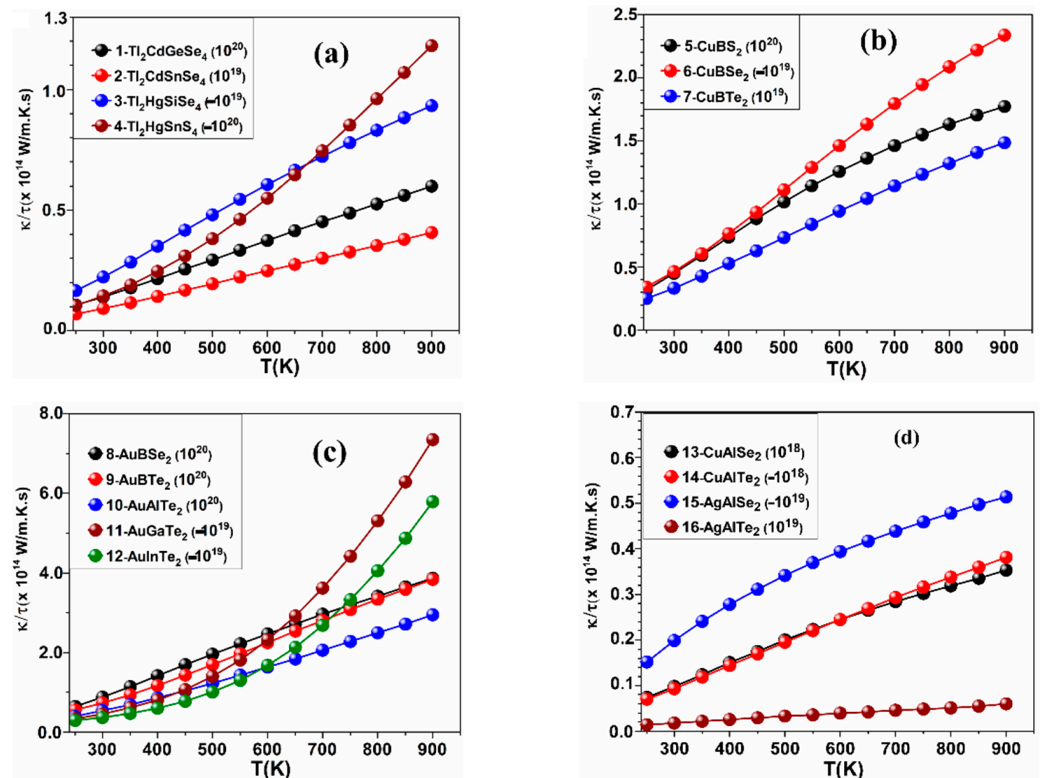
Figure 3. Calculated $\kappa ele/\tau$ the temperature for (**a**) the crystals 1–4, (**b**) the crystals 5–7, (**c**) the crystals 8–12, and (**d**) the crystals 13–16.

The chemical potential-dependent transport properties of the crystals: 19-CuGaTe$_2$, 22-AgGaTe$_2$, 25-CuInTe$_2$, and 28-AgInTe$_2$ were calculated and can be found in the Supplementary Materials. Here, we focus only on the calculated *S* and *ZT* versus the temperature for these crystals at two wide ranges of carrier concentrations to reveal which one leads to a higher *S* and *ZT*. The ranges are: ($+2 \times 10^{19}$, $+8 \times 10^{19}$ in e$^-$/cm^3) and ($+2 \times 10^{18}$, $+8 \times 10^{18}$ in e$^-$/cm^3). Figure S11a–d shows *S* versus temperature for the crystals 19-CuGaTe$_2$ and 22-AgGaTe$_2$ over the two different ranges of *n*. *S* can reach its maximum value for the crystal 22-AgGaTe$_2$ ($S \approx 310$ μV/K) and for 19-CuGaTe$_2$ ($S \approx 320$ μV/K) at 650 K when $n = 2 \times 10^{19}$ for both these two crystals. In contrast, *S* can reach its maximum value at 450 K for 22-AgGaTe$_2$ ($S \approx 325$ μV/K) and at 400 K for 19-CuGaTe$_2$ ($S \approx 400$ μV/K) when $n = 2 \times 10^{18}$ for both crystals. Figure S11e–h shows our results for *ZT* at these two different ranges of *n*. For the crystals 19-CuGaTe$_2$ and 22-AgGaTe$_2$, in the first range, *ZT* hits its maximum value ($ZT \approx 0.8$) at 500 K for the crystal 22-AgGaTe2 and at 450 K ($ZT \approx 0.82$) for the crystal 19-CuGaTe$_2$ when $n = 2 \times 10^{19}$ for both these two crystals. While when $n = 8 \times 10^{19}$, *ZT* has its highest value at 900 K for both crystals. For the same crystals, but in the second range of carrier concentrations, *ZT* reaches its maximum values ($ZT \approx 0.86$ for 22-AgGaTe$_2$, $ZT \approx 0.88$ for 19-CuGaTe$_2$) at 350 K when $n = 2 \times 10^{18}$ for both crystals. For the crystals 25-CuInTe$_2$ and 28-AgInTe$_2$ at the first range of *n*, the situation is a bit different. *ZT* versus *T* for these two crystals is shown in Figure S12. *ZT* for 28-AgInTe$_2$

starts from its minimum value at 250 K then increases with increasing temperature to reach a maximum value ($ZT \approx 0.4$) at 700 K when $n = 3 \times 10^{19}$, then it starts decreasing. However, at 250 K, when $n = 5 \times 10^{19}$ ZT starts from its maximum value ($ZT \approx 0.84$), it starts decreasing rapidly with increasing temperature. ZT for 25-$CuInTe_2$ starts from its minimum value at 250 K then increases with increasing temperature to reach maximum value ($ZT \approx 0.4$) at 600 K when $n = 4 \times 10^{19}$ then starts decreasing, while ZT starts from its maximum value ($ZT \approx 0.84$) at 250 K when $n = 6 \times 10^{19}$ then starts decreasing rapidly with increasing temperature. These are totally new findings that have not been revealed yet in any previous work.
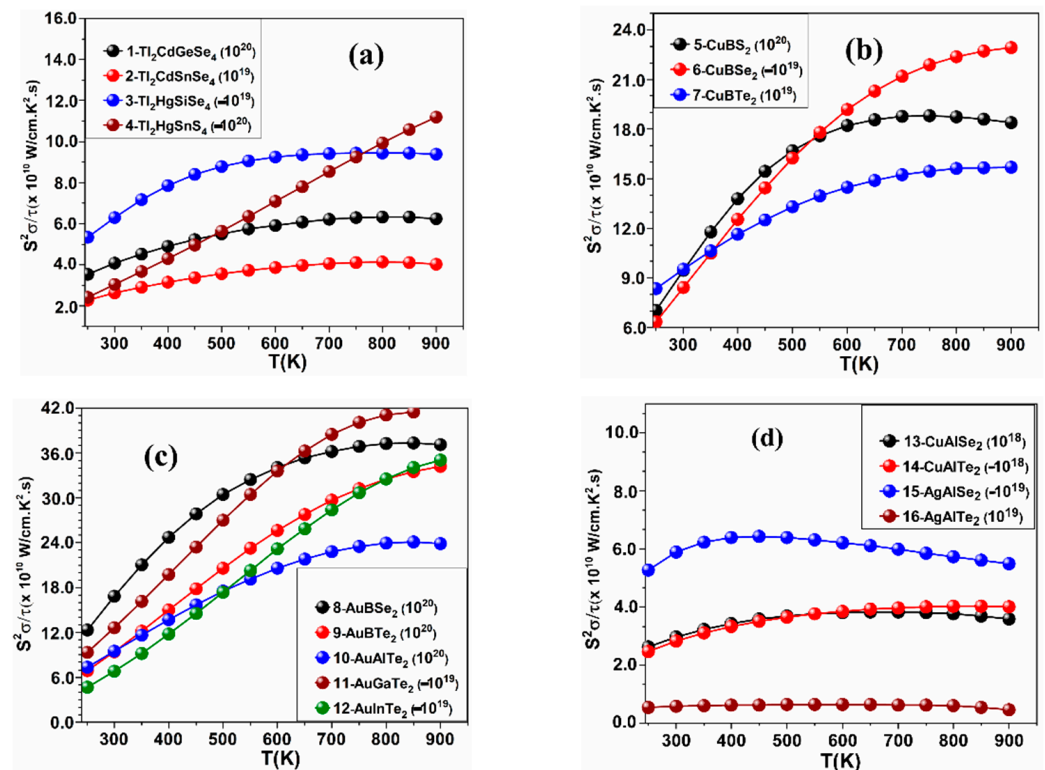
Figure 4. Calculated PF versus the temperature for (**a**) the crystals 1–4, (**b**) the crystals 5–7, (**c**) the crystals 8–12, and (**d**) the crystals 13–16.

It is not easy to find previous experimental studies on the thermoelectric properties of these 30 crystals. Nevertheless, we have identified the following available experimental data. A study by Gui etc. [109] showed that ZT values at 850 K are 1.1, 0.87, and 1.0 for $CuInS_2$, $CuInSe_2$, and $CuInTe_2$ crystals, respectively. Furthermore, our calculated ZT at 850 K was 0.65, 0.6, and 0.5 for these three crystals, respectively. Another four experimental studies [45,110–112] were conducted on the thermoelectric properties of $CuInTe_2$ crystal. The first two studies showed that $ZT \approx 0.6$ at 800 K, which is very close to ours ($ZT = 0.56$ at 800 K). The third and fourth studies showed that $ZT \approx 0.35$ and $ZT \approx 0.4$ at 700 K, which is less than ours ($ZT = 0.69$ at 700 K). Another two experimental studies [113,114] were carried out on the thermoelectric properties of $CuGaTe_2$ crystal. Ref. [113] reported $ZT \approx 1.12$ at 900 K, which is higher than our results ($ZT = 0.67$ at 900 K), while Ref. [114] showed that $ZT \approx 0.9$ at 850 K, which is comparable to ours ($ZT \approx 0.7$ at 850 K). On the other hand, Cao et al. and Yusufu et al. [58,115] experimentally found that ZT for $AgGaTe_2$ to be about 0.5 at 800 K and 0.4 at 850 K, less than ours ($ZT = 0.729$ at 800, $ZT = 0.724$ at 850).
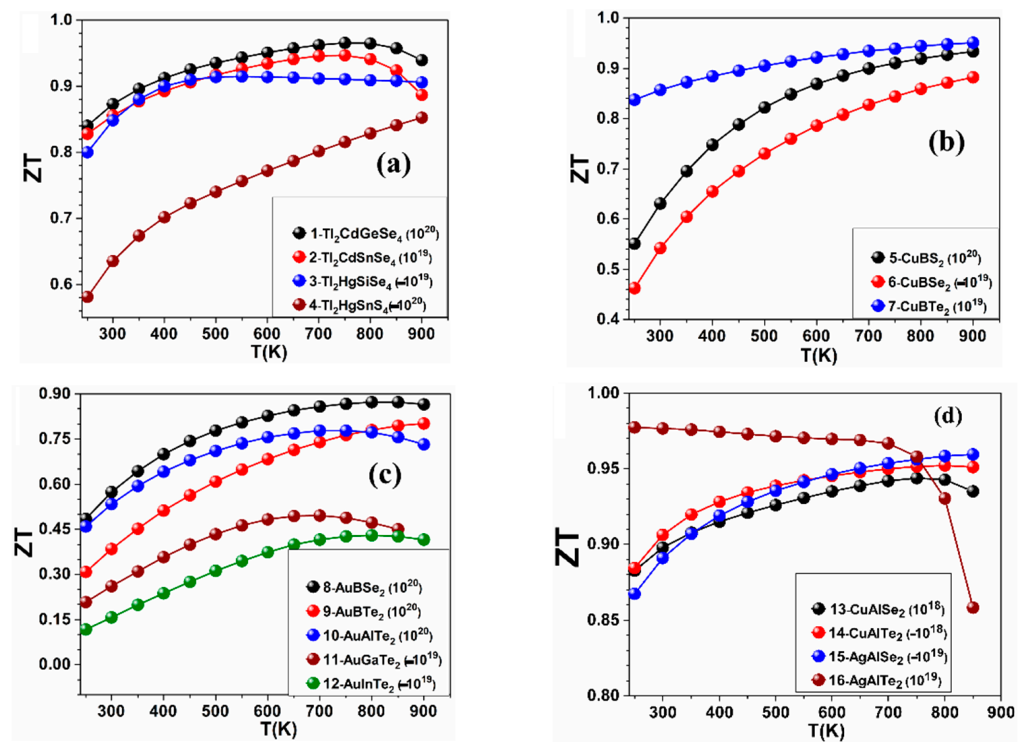
Figure 5. Calculated *ZT* versus the temperature for (**a**) the crystals 1–4, (**b**) the crystals 5–7, (**c**) the crystals 8–12, and (**d**) the crystals 13–16.

3.2. Transport Properties of AgSbSe$_2$ and AgSbTe$_2$ Crystals and the Doped Ones: AgSb$_{0.94}$Cd$_{0.06}$Te$_2$ and AgSbTe$_{1.85}$Se$_{0.15}$
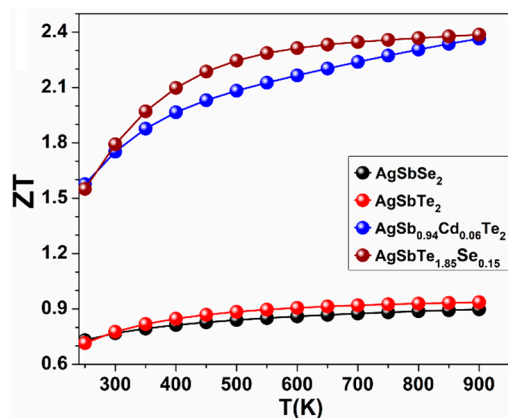
Cd-doped and Se-doped crystals (AgSb$_{0.94}$Cd$_{0.06}$Te$_2$ and AgSbTe$_{1.85}$Se$_{0.15}$) arise from the substitution of Cd and Se atoms in AgSbTe$_2$ crystal (Figure 6). The dopant compositions of AgSb$_{0.94}$Cd$_{0.06}$Te$_2$ and AgSbTe$_{1.85}$Se$_{0.15}$ were chosen carefully based on very recent experimental study [46]. Our calculations for the band structure of AgSbSe$_2$ and AgSbTe$_2$ crystals showed that these crystals are semi-metallic materials. Our calculations for *ZT* are shown in Table 2, while Figures 7 and 8 show our calculations for *ZT*, *S*, *σ*, *κ*$_{ele}$, and PF as a function of temperature for the pure AgSbSe$_2$ and AgSbTe$_2$ crystals and for the doped ones (AgSb$_{0.94}$Cd$_{0.06}$Te$_2$ and AgSbTe$_{1.85}$Se$_{0.15}$).
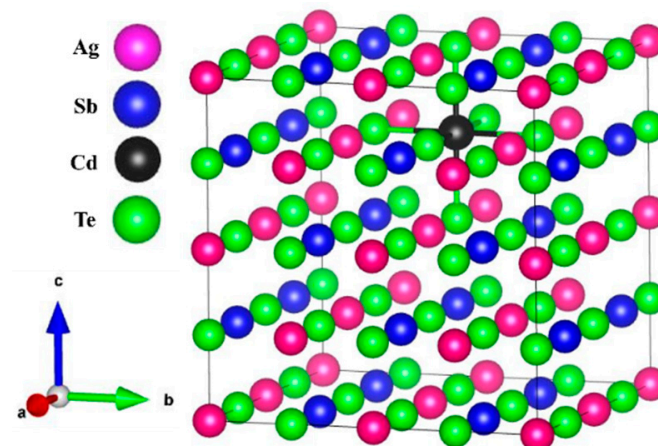

Figure 6. The crystal structure of AgSb$_{0.94}$Cd$_{0.06}$Te$_2$ crystal.

Table 2. Our calculated ZT at 900 K and a comparison with other experimental works for the pure AgSbSe$_2$ and AgSbTe$_2$ crystals, and the doped ones: AgSb$_{0.94}$Cd$_{0.06}$Te$_2$ and AgSbTe$_{1.85}$Se$_{0.15}$.

Crystal	n	ZT (Ours)	ZT
AgSbSe$_2$	10^{20}	0.898(750 K)	0.41(650 K) [71], 0.65(675 K) [116]
AgSbTe$_2$	10^{19}	0.924(750 K)	1.2(650 K) [47], 0.9(675 K) [76]
AgSb$_{0.94}$Cd$_{0.06}$Te$_2$	9.0×10^{19}	2.36(700 K)	2.6(573 K) [46]
AgSbTe$_{1.85}$Se$_{0.15}$	10^{20}	2.39(700 K)	2.1(575 K) [21,47]

Figure 7. Calculated *ZT* versus the temperature for the pure AgSbSe$_2$ and AgSbTe$_2$ crystals, and the doped ones: AgSb$_{0.94}$Cd$_{0.06}$Te$_2$ and AgSbTe$_{1.85}$Se$_{0.15}$.
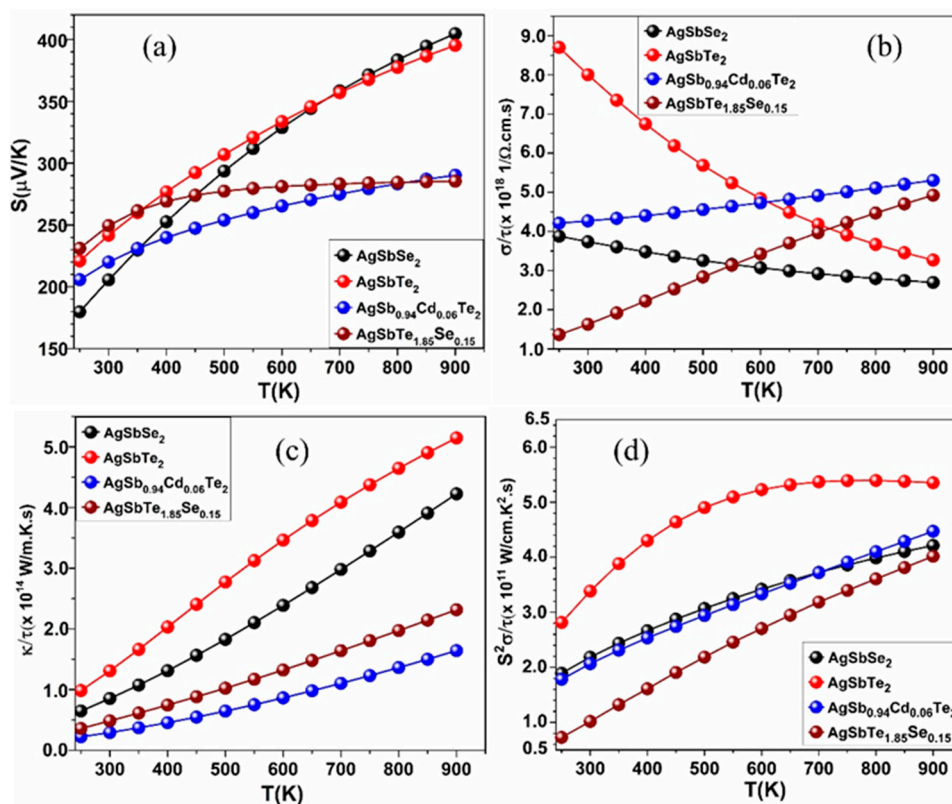
Figure 8. Calculated S, σ, κ_{ele}, and PF versus the temperature for the pure AgSbSe$_2$ and AgSbTe$_2$ crystals, and the doped ones: AgSb$_{0.94}$Cd$_{0.06}$Te$_2$ and AgSbTe$_{1.85}$Se$_{0.15}$. (**a**) is for S, (**b**) is for σ, (**c**) is for κ_{ele}, and (**d**) is for PF.

As can be seen from these figures, $AgSb_{0.94}Cd_{0.06}Te_2$ and $AgSbTe_{1.85}Se_{0.15}$ crystals have less S and higher σ than the pure ones. Experimentally, S Roychowdhury et al. [46] showed that the hole concentration at 300 K of the pure $AgSbTe_2$ increased from 4.3×10^{19} cm^{-3} to 8.3×10^{19} cm^{-3} when doped with 6 mol% Cd($AgSb_{0.94}Cd_{0.06}Te_2$), and that was the reason for reducing S values ($S = \propto 1/n$) and increasing values of σ ($\sigma \propto n$). Our study showed the same behavior for S. The doped crystals have less κ_{ele} than the pure ones at high temperatures, and this makes the doped crystals have higher ZT than the pure crystals. This implies that doping by Cd and Se atoms results in reduced thermal conductivity and increases the TE performance. In addition, we contend that increasing the carrier concentration (n) does not necessarily mean an increase in the values of κ_{ele} for the doped crystals. This can be true both experimentally and computationally since, in some cases, the doping process can create point defects, vacancies, and distortion in the bonding between atoms. This may lead to the reduction in the heat energy transferred by the charge carriers (electrons) or the phonons in the doped crystals.

Thermal conductivity has two components: lattice (phonons) and charge carriers. Increasing carrier concentration will increase thermal conductivity (if lattice does not change). However, for the dependence on temperature (our case), things may become more complicated. According to our DFT calculations, the crystals $AgSbSe_2$ and $AgSbTe_2$ are metallic materials with zero energy band gap. Wiedemann-Franz law basically relates the two conductivities of metals, i.e., thermal (κ_{ele}) and electrical (σ) conductivity with temperature. It states that the ratio of thermal conductivity κ_{ele} and electrical conductivity σ is proportional to the temperature of the specimen. G. Wiedemann and R. Franz established (based on experimental data) that the ratio $\frac{\kappa_{ele}}{\sigma}$ is constant at a constant temperature. L. Lorenz demonstrated that the relation $\frac{\kappa_{ele}}{\sigma}$ changes in direct proportion to the absolute temperature T, $\frac{\kappa_{ele}}{\sigma} = LT$, where T = temperature, $L = 2.54 \times 10^{-8}$ WΩ/K^2, Lorentz number (a constant). This law basically states that with an increase in temperature, the thermal conductivity of metals increases while the electrical conductivity decreases. These two properties of metals are dependent on the free electrons. An increase in temperature increases the average velocity of the free electrons leading to an increase in heat energy transfer. On the other hand, an increase in the velocity of electrons also increases the number of collisions of the free electrons with lattice ions and hence contributes to an increase in electrical resistivity or reduction in electrical conductivity (σ), and this what can be noticed in Figure 8b,c for the crystals $AgSbSe_2$ and $AgSbTe_2$. However, this law has certain limitations. The proportionality does not hold true for all ranges of temperature. It is only found valid for very high temperatures and very low temperatures.

The above argument can be valid for the metallic materials, but few experimental studies showed that $AgSbSe_2$ and $AgSbTe_2$ crystals are semiconductors with a very narrow energy band gap. When we have semiconductors, alloys, or other interesting structures, the issue is much more complex, and it is difficult to obtain a general dependence of the conductivities with the temperature. That means the relationship between the thermal and electrical conductivities in the case of semiconducting materials is very complicated and is different from one material to another. Many researchers have tried to find a common formula that correlates between the two types of conductivities, and this relationship is still under study till now.

The effective charge (Q*) on each atom of these four crystals is represented in Table 3, while Figure 9 shows the BO versus bond length (BL) for these four crystals. It is extremely helpful to investigate the interatomic bond strength between every pair of atoms in the crystal as represented by the BO values [92]. Important insights are revealed in Figure 9 and Table 3. In the $AgSbSe_2$ crystal, there are two bonds: Ag-Se and Sb-Se, and these two bonds are ionic bonds (metal-nonmetal bonds) where the two metal elements (Ag, Sb) lose charge to the nonmetal chalcogen element (Se). While in the $AgSbTe_2$ crystal, there are also two bonds: Ag-Te and Sb-Te, but the Ag-Te and Sb-Te bonds are more complicated to explain because Te is a metalloid element. Te sometimes acts similarly to a metal element and loses charge, and in different cases, it acts similarly to a nonmental element and gains

charge (as our calculations show). As can be seen in Figure 9a,c, the Ag-Te bond is much stronger than the Ag-Se, Sb-Se, and Sb-Te bonds. The chalcogen elements (Se, Te) in each crystal of $AgSbSe_2$ and $AgSbTe_2$ make bonds with two atoms (two bond types): Ag and Sb. While each atom: Ag or Sb has just one bond type: Ag-Se and Sb-Se in $AgSbSe_2$, and Ag-Te and Sb-Te in $AgSbTe_2$. From the oxidation states of the Ag and Sb atoms, we know that each atom of these two atoms can bond with more than one or more different atoms in the crystal structure, and this leads to the fact that these two atoms can vibrate with higher frequency for phonons (higher thermal conductivity and less TE performance) than when they make two or three bonds with two or three other atoms in the crystal.

Table 3. Calculated average effective charge for pure $AgSbSe_2$ and $AgSbTe_2$ crystals, and the doped ones: $AgSb_{0.94}Cd_{0.06}Te_2$ and $AgSbTe_{1.85}Se_{0.15}$.

#	Crystal	Q* (in e$^-$)
1	$AgSbSe_2$	10.971(Ag), 4.399(Sb), 6.315(Se)
2	$AgSbTe_2$	11.102(Ag), 4.694(Sb), 6.102(Te)
3	$AgSb_{0.94}Cd_{0.06}Te_2$	11.080(Ag), 4.748(Sb), 11.243(Cd), 6.102(Te)
4	$AgSbTe_{1.85}Se_{0.15}$	11.030(Ag), 4.712(Sb), 6.120(Te), 6.266(Se)
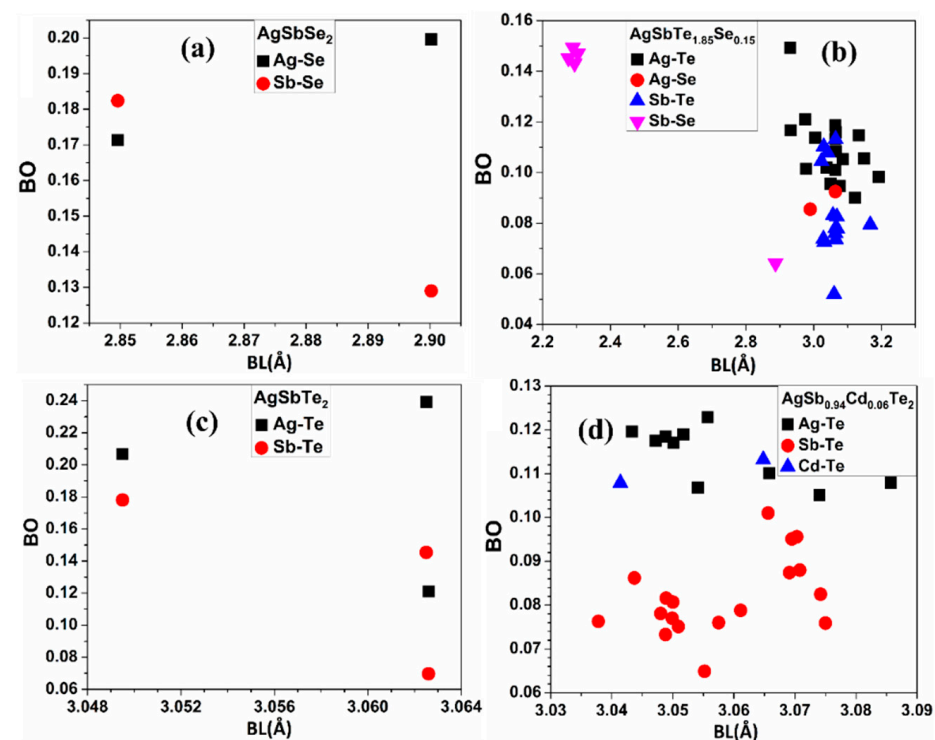
Figure 9. Calculated BO versus BL for the pure $AgSbSe_2$ and $AgSbTe_2$ crystals, and the doped ones: $AgSb_{0.94}Cd_{0.06}Te_2$ and $AgSbTe_{1.85}Se_{0.15}$: (**a**) BO versus BL for $AgSbSe_2$, (**b**) BO versus BL for $AgSbTe_{1.85}Se_{0.15}$, (**c**) BO versus BL for $AgSbTe_2$, and (**d**) BO versus BL for $AgSb_{0.94}Cd_{0.06}Te_2$.

When the $AgSbTe_2$ crystal is doped with Se atoms ($AgSbTe_{1.85}Se_{0.15}$), we notice from Figure 9b that each atom, Ag or Sb, now has two bond types and is bonded with two atoms (Se and Te) instead of just one atom, which we could not see in the pure $AgSbTe_2$. Similarly, Figure 9d for the Te-doped crystal ($AgSb_{0.94}Cd_{0.06}Te_2$) shows that the Te atom (heavy atom) is bonded now with three atoms (Ag, Sb, and Cd) instead of just two atoms (Ag and Sb) in the pure $AgSbTe_2$. These three bonds in $AgSb_{0.94}Cd_{0.06}Te_2$ make the heavy Te atom more bound and vibrate with lower frequencies for phonons. Hence, there is less thermal conductivity and higher TE performance. We conclude that the doping process of the $AgSbTe_2$ crystal by Se and Cd dopants created new three bonds (Ag-Se, Sb-Se, and Cd-Te

(Figure 8b–d) for atoms Ag, Sb, and Te and made them vibrate with lower frequencies for phonons (less thermal conductivity and higher TE performance) than in pure $AgSbTe_2$, and this may explain why $AgSbTe_{1.85}Se_{0.15}$ and $AgSb_{0.94}Cd_{0.06}Te_2$ crystals have less thermal conductivity and much higher ZT than the pure $AgSbTe_2$ in terms of bonding properties.

Thermal conductivity in thermoelectric materials comes from two sources: (1) electrons and holes transporting heat (κ_{ele}) and (2) phonons traveling through the lattice (κ_{lat}). Most of the electronic term (κ_{ele} is directly related to the electrical conductivity through the Wiedemann–Franz law:

$$\kappa = \kappa_{ele} + \kappa_{lat} \tag{8}$$

$$\kappa_{ele} = L\sigma T = LnemT \tag{9}$$

The Lorenz factor can vary, particularly with carrier concentration. Accurate assessment of κ_{ele} is important, as κ_{lat} is often computed as the difference between κ and κ_{ele} (Equation (8)) using the experimental electrical conductivity. A common source of uncertainty in κ_{ele} occurs in low-carrier-concentration materials where the Lorenz factor can be reduced by as much as 20% from the free-electron value. Additional uncertainty in κ_{ele} arises from mixed conduction, which introduces a bipolar effect term into the thermal conductivity [117]. S Roychowdhury et al. [46] showed that the values of κ_{lat} are in the range 0.5–0.55 W/m.K and in the range 0.1–0.13 W/m.K at the temperature range 300–575 K for the two crystals $AgSbTe_2$ and $AgSb_{0.94}Cd_{0.06}Te_2$ respectively. In contrast, our calculations showed that the values of κ_{ele} are in the range 1.0–3.3 W/m.K and in the range 0.3–0.75 W/m.K at the temperature range 250–600 K for the two crystals AgSbTe2 and $AgSb_{0.94}Cd_{0.06}Te_2$ respectively. This can be used as evidence that κ_{ele} has a bigger effect on TE performance than κ_{lat}. A further calculation of κ_{lat} will help to explore why the doped crystals have much higher TE performance than the pure ones, which is not the focus of our study at this stage.

3.3. Correlation between Transport and Bonding Properties in 30 Chalcogenide Crystals

Identifying the underlying correlation between the TE performance (*ZT*) and the bonding characteristics of the 30 chalcogenide crystals is one of the main objectives of this work. In this regard, exploring the connection between the thermoelectric properties of the 30 crystals and the TBOD could be revealing. TBOD values for all 30 crystals are represented in Table S2 in the SI. TBOD describes the internal cohesion of the crystal, so that higher TBOD may imply a reduced value of thermal conductivity. In Figure S13, we plot the *ZT* versus TBOD for the 30 crystals. We notice that there is a general trend where *ZT* increases with the increase in TBOD. This correlation between TBOD and *ZT* could be revealed for the first time in this work. However, the crystals inside the blue circle shape ($Tl_2CdGeSe_4$, $Tl_2CdSnSe_4$, $Tl_2HgSiSe_4$, Tl_2HgSnS_4, $NaInSe_2$, and $NaInTe_2$) deviate from this trend. To explain this deviation, we plotted BO versus BL (Figure 10) for three crystals that deviate from the trend ($Tl_2CdGeSe_4$, $Tl_2CdSnSe_4$, and $Tl_2HgSiSe_4$) and for three crystals that follow the trend ($CuBS_2$, $CuBSe_2$, and $CuBTe_2$). From Figure 10, $Tl_2CdGeSe_4$, $Tl_2CdSnSe_4$, and $Tl_2HgSiSe_4$ crystals have much lower TBOD values than $CuBS_2$, $CuBSe_2$, and $CuBTe_2$ crystals, but they still have larger values of *ZT* than $CuBS_2$, $CuBSe_2$, and $CuBTe_2$ crystals. It is true that $Tl_2CdGeSe_4$, $Tl_2CdSnSe_4$, and $Tl_2HgSiSe_4$ crystals have much lower TBOD values than $CuBS_2$, $CuBSe_2$, and $CuBTe_2$ crystals, but at the same time, they have much smaller values of κ_{ele} than $CuBS_2$, $CuBSe_2$, and $CuBTe_2$ crystals, and this is the reason why $Tl_2CdGeSe_4$, $Tl_2CdSnSe_4$, and $Tl_2HgSiSe_4$ crystals still have higher values of *ZT* than $CuBS_2$, $CuBSe_2$, and $CuBTe_2$ crystal (which have larger values of κ_{ele}). The same explanation is valid for the other crystals ($NaInSe_2$ and $NaInTe_2$).

The crystal 19-$CuGaTe_2$ has higher *ZT* (*ZT* = 0.662 at 900 K) than the crystal 18-$CuGaSe_2$ (*ZT* = 0.556 at 900 K). The same trend can be seen in the crystals 27-$AgInSe_2$ to 28-$AgInTe_2$, where 28-$AgInTe_2$ has *ZT* = 0.605 at 900 K while 27-$AgInSe_2$ has *ZT* = 0.243 at the same temperature. In all these crystals, *ZT* decreases when moving from Te-related crystals toward Se-related crystals. In some crystals, this behavior can be related to the

heavy Te atom, which results in less thermal conductivity and higher *ZT*. One of the important parameters that can affect the value of thermal conductivity is the bonding nature of the atoms in the crystal. Weaker bonds (lower bond order (BO)) imply higher energy phonon vibrations and, therefore, a higher value of κ and a reduced value of *ZT*. In contrast, stronger bonds (higher BO) imply smaller energy phonon vibrations and a reduced value of κ, and a higher value of *ZT*. Bonding properties calculations for these crystals have already been published in our previous work [79], and Table 4 represents our calculations for the bonding properties of the above crystals. As can be seen from Table 4, The crystals 19-CuGaTe$_2$ and 28-AgInTe$_2$ have bonds with higher bond order (stronger bonds) than the crystals 18-CuGaSe$_2$ and 27-AgInSe$_2$, and we believe that this is one of the main reasons that 19-CuGaTe$_2$ and 28-AgInTe$_2$ have smaller κ and higher *ZT* than the crystals: 18-CuGaSe$_2$ and 27-AgInSe$_2$.
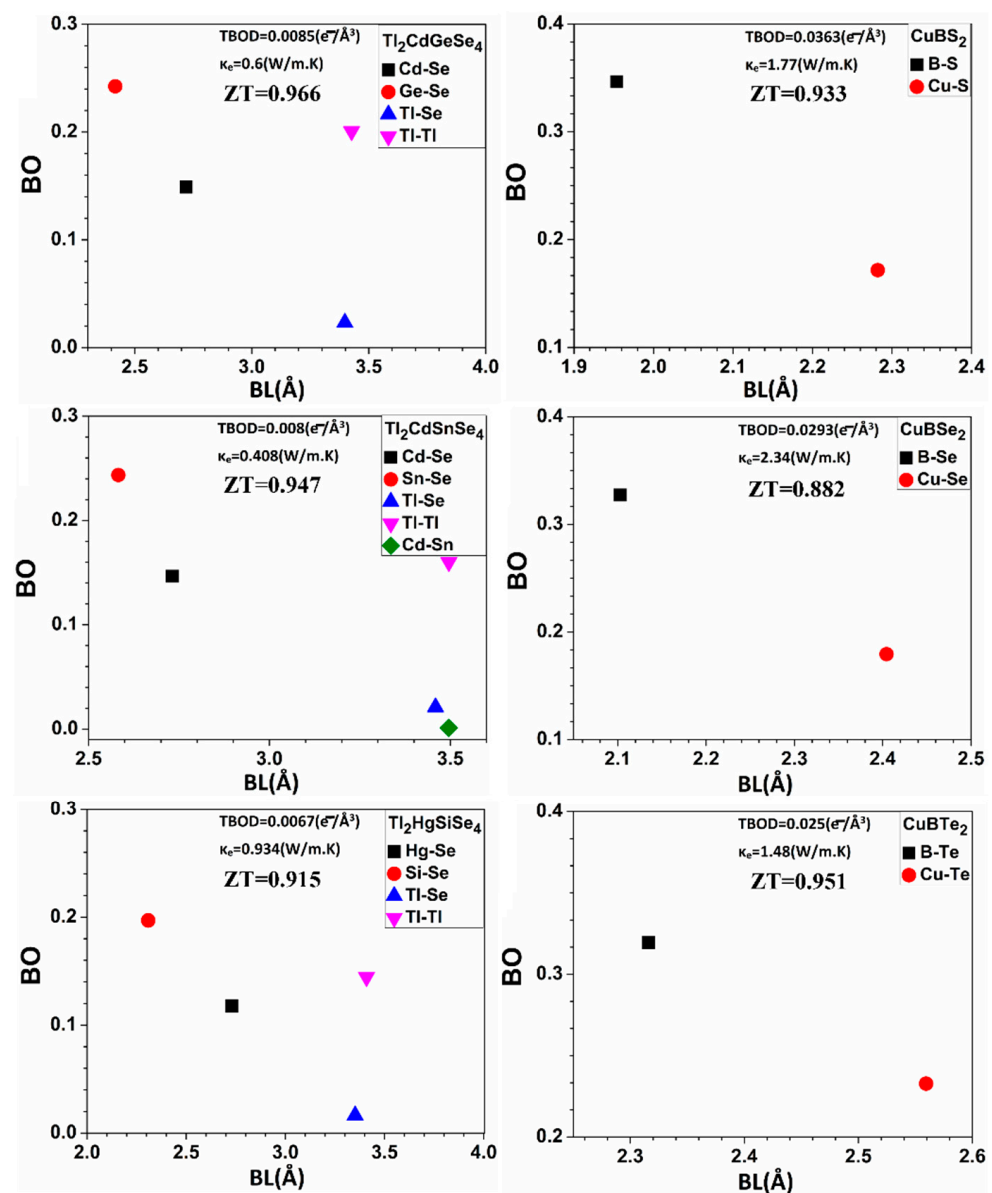

Figure 10. BO versus BL for the three crystals: (Tl$_2$CdGeSe$_4$, Tl$_2$CdSnSe$_4$, and Tl$_2$HgSiSe$_4$), and for the three crystals: (CuBS$_2$, CuBSe$_2$, and CuBTe$_2$).

Table 4. Bonding properties of 18-CuGaSe$_2$, 19-CuGaTe$_2$, 27-AgInSe$_2$, and 28-AgInTe$_2$ crystals.

CuGaSe$_2$			CuGaTe$_2$		
bond	**BL(Å)**	**BO**	**bond**	**BL(Å)**	**BO**
Cu-Se	2.4315	0.1916	Cu-Te	2.5937	0.2286
Ga-Se	2.4746	0.2572	Ga-Te	2.6878	0.2709
AgInSe$_2$			AgInTe$_2$		
bond	**BL(Å)**	**BO**	**bond**	**BL(Å)**	**BO**
Ag-Se	2.6727	0.1530	Ag-Te	2.8134	0.1814
In-Se	2.6558	0.2384	In-Te	2.8603	0.2581

4. Conclusions

A computational study was performed to investigate: 1. the thermoelectric transport properties of 30 chalcogenide crystals to provide a large set of thermoelectric transport data, which can be a good start to explore their further potentials both experimentally and theoretically, and 2. the temperature-dependent transport properties of the pure AgSbSe$_2$ and AgSbTe$_2$ and doped AgSb$_{0.94}$Cd$_{0.06}$Te$_2$ and AgSbTe$_{1.85}$Se$_{0.15}$ crystals. In the first part (the 30 crystals), the transport properties of the crystals: 1-Tl2CdGeSe$_4$, 2-Tl2CdSnSe$_4$, 3-Tl$_2$HgSiSe$_4$, 4-Tl$_2$HgSnS$_4$, 8-AuBSe$_2$, 9-AuBTe$_2$, 10-AuAlTe$_2$, 11-AuGaTe$_2$, 12-AuInTe$_2$, 15-AgAlSe$_2$, and 16-AgAlTe$_2$ are investigated for the first time. These eleven chalcogenide crystals are promising thermoelectric materials which have high Seebeck coefficients and a high figure of merit. For the crystals 19-CuGaTe$_2$ and 22-AgGaTe$_2$, we conclude that the second range of *n*: (+2 × 10^{18}, +8 × 10^{18} in e$^-$/cm^3) leads to much better TE performance at low temperatures than the first range of *n*: (+2 × 10^{19}, +8 × 10^{19} in e$^-$/cm^3). In the second part, it is found that the *ZT* value improves significantly, higher than 2.0 in p-type doped AgSb$_{0.94}$Cd$_{0.06}$Te$_2$ and AgSbTe$_{1.85}$Se$_{0.15}$ crystals. Our calculations show a difference in the calculated values of the Seebeck coefficient and figure of merit for some crystals compared to other previous experimental and theoretical studies. Some correlations between the calculated bonding nature of these crystals and their thermoelectric properties were revealed in this work.

Despite a large number of simplified calculations on complex thermal transport properties, some for the first time, there are obviously some serious drawbacks, such as ignoring the lattice thermal conductivity. We are encouraged by the current results and aspire to continue research in this area for more complex and interesting chalcogenide crystals. It is desirable to improve the DFT calculations with better options, such as using either hybrid potential or Becke–Johnson potential. We should also point out that there are cases [65,118] where the neglect of SOC may not result in too large a difference due to unpredictable fluctuations. Our results without SOC are within the limit of these fluctuations and will still be useful as a first step to more accurate calculations. Enhancing the thermoelectric performance of these crystals can be achieved by decreasing the values of the thermal conductivity, which is our vision for future works. This could be performed by making these crystals as 2D and 1D materials.

Supplementary Materials: The following supporting information can be downloaded at: https://www.mdpi.com/article/10.3390/ma15082843/s1, Figure S1: Calculated Seebeck coefficient (S) versus the chemical potential for the crystals from 1-Tl$_2$CdGeS$_4$ to 16-AgAlTe$_2$; Figure S2: Calculated PF versus the chemical potential for the crystals from 1-Tl$_2$CdGeS4 to 16-AgAlTe$_2$; Figure S3: Calculated Seebeck coefficient (S) versus the chemical potential for the crystals from 17-CuGaS$_2$ to 30-NaInTe$_2$; Figure S4: Calculated PF versus the chemical potential for the crystals from 17-CuGaS$_2$ to 30-NaInTe$_2$; Figure S5: Calculated σ/τ versus the chemical potential for the 30 crystals; Figure S6: Calculated κ/τ versus the chemical potential for the 30 crystals; Figure S7: Calculated ZT versus the chemical potential; Figure S8: Calculated σ/τ versus the temperature for the crystals 13–16; Figure S9: Calculated S and PF versus the temperature for the crystals from 17 to 30; Figure S10: Calculated ZT versus the temperature for the crystals from 17 to 30; Figure S11: S and ZT versus the temperature

for the crystals: (a,b,e,f) are for 19-CuGaTe2 crystal, and (c,d,g,h) are for 22-AgGaTe2 crystal at two different ranges of *n*; Figure S12: Shows our results for ZT versus temperature at range of *n*: ($+2 \times 10^{19}$, $+8 \times 10^{19}$ in e-/cm^3) for the crystals 25-CuInTe2 and 28-AgInTe2; Figure S13: Calculated TBOD versus ZT for the 30 crystals. Table S1: The fully optimized structures with the corresponding experimental lattice parameters of 30 chalcogenide crystals; Table S2: Energy gap (Eg) (calculated in our previous works), the Seebeck coefficients (S), and figure of merit (ZT) as a function of chemical potential at room temperature (300 K), and the TBOD for these 30 chalcogenide crystals. In the previous published works (Refs. [79,80] in the main text), OLCAO code was used to calculate the energy band gap. Spin–Orbit Coupling (SOC) effect was not included in the calculations [119–122].

Author Contributions: W.-Y.C. conceived and directed the project. S.H. performed the calculations. S.H. made all figures. S.H., S.S., K.B., P.R., W.-Y.C. and N.L. drafted the paper. All authors participated in the discussion and interpretation of the results. All authors edited and proofread the final manuscript. All authors have read and agreed to the published version of the manuscript.

Institutional Review Board Statement: Not applicable.

Informed Consent Statement: Not applicable.

Data Availability Statement: The data used to support the findings of this study are included within the article.

Conflicts of Interest: The authors declare no conflict of interest.

References

1. Khan, S.A.; Azam, S. Electronic structure and thermoelectric properties of PbS1-xTex (x = 0, 0.25, 0.50, 0.75, 1.0) alloys: Ab initio study. *Superlattices Microstruct.* **2018**, *124*, 248–256. [CrossRef]
2. Rull-Bravo, M.; Moure, A.; Fernández, J.; Martín-González, M. Skutterudites as thermoelectric materials: Revisited. *RSC Adv.* **2015**, *5*, 41653–41667. [CrossRef]
3. Tan, G.; Zhao, L.-D.; Kanatzidis, M.G. Rationally designing high-performance bulk thermoelectric materials. *Chem. Rev.* **2016**, *116*, 12123–12149. [CrossRef] [PubMed]
4. Pichanusakorn, P.; Kuang, Y.; Patel, C.; Tu, C.; Bandaru, P. Feasibility of enhancing the thermoelectric power factor in GaN$_x$ As$_{1-x}$. *Phys. Rev. B* **2012**, *86*, 085314. [CrossRef]
5. Ouardi, S.; Fecher, G.H.; Felser, C.; Schwall, M.; Naghavi, S.S.; Gloskovskii, A.; Balke, B.; Hamrle, J.; Postava, K.; Pištora, J. Electronic structure and optical, mechanical, and transport properties of the pure, electron-doped, and hole-doped Heusler compound CoTiSb. *Phys. Rev. B* **2012**, *86*, 045116. [CrossRef]
6. Kim, H.; Kaviany, M. Effect of thermal disorder on high figure of merit in PbTe. *Phys. Rev. B* **2012**, *86*, 045213. [CrossRef]
7. Kerdsongpanya, S.; Alling, B.; Eklund, P. Effect of point defects on the electronic density of states of ScN studied by first-principles calculations and implications for thermoelectric properties. *Phys. Rev. B* **2012**, *86*, 195140. [CrossRef]
8. Wang, D.; He, W.; Chang, C.; Wang, G.; Wang, J.; Zhao, L.-D. Thermoelectric transport properties of rock-salt SnSe: First-principles investigation. *J. Mater. Chem. C* **2018**, *6*, 12016–12022. [CrossRef]
9. Rowe, D.M. *Thermoelectrics Handbook: Macro to Nano*; CRC Press: Boca Raton, FL, USA, 2018.
10. Furlong, R.R.; Wahlquist, E.J. US space missions using radioisotope power systems. *Nucl. News* **1999**, *42*, 26–35.
11. Yang, J.; Caillat, T. Thermoelectric materials for space and automotive power generation. *MRS Bull.* **2006**, *31*, 224–229. [CrossRef]
12. Kraemer, D.; Poudel, B.; Feng, H.-P.; Caylor, J.C.; Yu, B.; Yan, X.; Ma, Y.; Wang, X.; Wang, D.; Muto, A. High-performance flat-panel solar thermoelectric generators with high thermal concentration. *Nat. Mater.* **2011**, *10*, 532–538. [CrossRef] [PubMed]
13. Naghavi, S.S.; He, J.; Xia, Y.; Wolverton, C. Pd$_2$Se$_3$ monolayer: A promising two-dimensional thermoelectric material with ultralow lattice thermal conductivity and high power factor. *Chem. Mater.* **2018**, *30*, 5639–5647. [CrossRef]
14. Bejan, A.; Kraus, A.D. *Heat Transfer Handbook*; John Wiley & Sons: Hoboken, NJ, USA, 2003; Volume 1.
15. Aliabad, H.R.; Ghazanfari, M.; Ahmad, I.; Saeed, M. Ab initio calculations of structural, optical and thermoelectric properties for CoSb$_3$ and ACo$_4$Sb$_{12}$ (A = La, Tl and Y) compounds. *Comput. Mater. Sci.* **2012**, *65*, 509–519. [CrossRef]
16. Yuan, K.; Sun, Z.; Zhang, X.; Gong, X.; Tang, D. A first-principles study of the thermoelectric properties of rhombohedral GeSe. *Phys. Chem. Chem. Phys.* **2020**, *22*, 1911–1922. [CrossRef]
17. Hoat, D. Comparative study of structural, electronic, optical and thermoelectric properties of GaS bulk and monolayer. *Philos. Mag.* **2019**, *99*, 736–751. [CrossRef]

18. Hoat, D.; Naseri, M.; Ponce-Perez, R.; Hieu, N.N.; Vu, T.V.; Rivas-Silva, J.; Cocoletzi, G.H. Reducing the electronic band gap of BN monolayer by coexistence of P (As)-doping and external electric field. *Superlattices Microstruct.* **2020**, *137*, 106357. [CrossRef]

19. Hoat, D.; Naseri, M.; Hieu, N.N.; Ponce-Pérez, R.; Rivas-Silva, J.; Cocoletzi, G.H. Transition from indirect to direct band gap in SiC monolayer by chemical functionalization: A first principles study. *Superlattices Microstruct.* **2020**, *137*, 106320. [CrossRef]

20. Naseri, M.; Hoat, D. Prediction of 2D Li_2X (X = Se, Te) monolayer semiconductors by first principles calculations. *Phys. Lett. A* **2019**, *383*, 125992. [CrossRef]

21. Hong, M.; Wang, Y.; Liu, W.; Matsumura, S.; Wang, H.; Zou, J.; Chen, Z.G. Arrays of planar vacancies in superior thermoelectric $Ge_{1-x-y}Cd_xBi_yTe$ with band convergence. *Adv. Energy Mater.* **2018**, *8*, 1801837. [CrossRef]

22. Tang, G.; Liu, J.; Zhang, J.; Li, D.; Rara, K.H.; Xu, R.; Lu, W.; Liu, J.; Zhang, Y.; Feng, Z. Realizing high thermoelectric performance below phase transition temperature in polycrystalline snse via lattice anharmonicity strengthening and strain engineering. *ACS Appl. Mater. Interfaces* **2018**, *10*, 30558–30565. [CrossRef]

23. Gayner, C.; Kar, K.K. Recent advances in thermoelectric materials. *Prog. Mater. Sci.* **2016**, *83*, 330–382. [CrossRef]

24. Ju, H.; Kim, M.; Kim, J. A facile fabrication of n-type Bi_2Te_3 nanowire/graphene layer-by-layer hybrid structures and their improved thermoelectric performance. *Chem. Eng. J.* **2015**, *275*, 102–112. [CrossRef]

25. Han, C.; Sun, Q.; Li, Z.; Dou, S.X. Thermoelectric enhancement of different kinds of metal chalcogenides. *Adv. Energy Mater.* **2016**, *6*, 1600498. [CrossRef]

26. Liu, M.L.; Chen, I.W.; Huang, F.Q.; Chen, L.D. Improved thermoelectric properties of Cu-doped quaternary chalcogenides of $Cu_2CdSnSe_4$. *Adv. Mater.* **2009**, *21*, 3808–3812. [CrossRef]

27. Sevik, C.; Çağın, T. Ab initio study of thermoelectric transport properties of pure and doped quaternary compounds. *Phys. Rev. B* **2010**, *82*, 045202. [CrossRef]

28. Ibáñez, M.; Zamani, R.; LaLonde, A.; Cadavid, D.; Li, W.; Shavel, A.; Arbiol, J.; Morante, J.R.; Gorsse, S.; Snyder, G.J. $Cu_2ZnGeSe_4$ nanocrystals: Synthesis and thermoelectric properties. *J. Am. Chem. Soc.* **2012**, *134*, 4060–4063. [CrossRef]

29. Zeier, W.G.; Heinrich, C.P.; Day, T.; Panithipongwut, C.; Kieslich, G.; Brunklaus, G.; Snyder, G.J.; Tremel, W. Bond strength dependent superionic phase transformation in the solid solution series $Cu_2ZnGeSe_{4-x}S_x$. *J. Mater. Chem. A* **2014**, *2*, 1790–1794. [CrossRef]

30. Navrátil, J.; Kucek, V.; Plecháček, T.; Černošková, E.; Laufek, F.; Drašar, Č.; Knotek, P. Thermoelectric Properties of $Cu_2HgSnSe_4$-$Cu_2HgSnTe_4$ Solid Solution. *J. Electron. Mater.* **2014**, *43*, 3719–3725. [CrossRef]

31. Bekki, B.; Amara, K.; Marbouh, N.; Khelfaoui, F.; Benallou, Y.; Elkeurti, M.; Bentayeb, A. Theoretical study of structural, elastic and thermodynamic properties of Cu_2MgSnX_4 (X = S, Se and Te) quaternary compounds. *Comput. Condens. Matter* **2019**, *18*, e00339. [CrossRef]

32. Altosaar, M.; Raudoja, J.; Timmo, K.; Danilson, M.; Grossberg, M.; Krustok, J.; Mellikov, E. $Cu_2Zn_{1-x}Cd_xSn$ $(Se_{1-y}S_y)_4$ solid solutions as absorber materials for solar cells. *Physica Status Solidi (A)* **2008**, *205*, 167–170. [CrossRef]

33. Khyzhun, O.; Bekenev, V.; Ocheretova, V.; Fedorchuk, A.; Parasyuk, O. Electronic structure of $Cu_2ZnGeSe_4$ single crystal: Ab initio FP-LAPW calculations and X-ray spectroscopy measurements. *Phys. B Condens. Matter* **2015**, *461*, 75–84. [CrossRef]

34. Jiang, H.; Dai, P.; Feng, Z.; Fan, W.; Zhan, J. Phase selective synthesis of metastable orthorhombic Cu_2ZnSnS_4. *J. Mater. Chem.* **2012**, *22*, 7502–7506. [CrossRef]

35. Levcenco, S.; Dumcenco, D.; Huang, Y.; Arushanov, E.; Tezlevan, V.; Tiong, K.; Du, C. Polarization-dependent electrolyte electroreflectance study of Cu_2ZnSiS_4 and $Cu_2ZnSiSe_4$ single crystals. *J. Alloys Compd.* **2011**, *509*, 7105–7108. [CrossRef]

36. Li, Y.; Fan, W.; Sun, H.; Cheng, X.; Li, P.; Zhao, X. Electronic, optical and lattice dynamic properties of the novel diamond-like semiconductors Li_2CdGeS_4 and Li_2CdSnS_4. *J. Phys. Condens. Matter* **2011**, *23*, 225401. [CrossRef] [PubMed]

37. Steinhagen, C.; Panthani, M.G.; Akhavan, V.; Goodfellow, B.; Koo, B.; Korgel, B.A. Synthesis of Cu_2ZnSnS_4 nanocrystals for use in low-cost photovoltaics. *J. Am. Chem. Soc.* **2009**, *131*, 12554–12555. [CrossRef]

38. Guo, Q.; Ford, G.M.; Yang, W.-C.; Walker, B.C.; Stach, E.A.; Hillhouse, H.W.; Agrawal, R. Fabrication of 7.2% efficient CZTSSe solar cells using CZTS nanocrystals. *J. Am. Chem. Soc.* **2010**, *132*, 17384–17386. [CrossRef]

39. Chen, S.; Gong, X.; Walsh, A.; Wei, S.-H. Electronic structure and stability of quaternary chalcogenide semiconductors derived from cation cross-substitution of II-VI and I-III-VI_2 compounds. *Phys. Rev. B* **2009**, *79*, 165211. [CrossRef]

40. Schnabel, T.; Löw, M.; Ahlswede, E. Vacuum-free preparation of 7.5% efficient Cu_2ZnSn $(S, Se)_4$ solar cells based on metal salt precursors. *Sol. Energy Mater. Sol. Cells* **2013**, *117*, 324–328. [CrossRef]

41. Fella, C.M.; Romanyuk, Y.E.; Tiwari, A.N. Technological status of Cu_2ZnSn $(S, Se)_4$ thin film solar cells. *Sol. Energy Mater. Sol. Cells* **2013**, *119*, 276–277. [CrossRef]

42. Vu, T.V.; Lavrentyev, A.; Gabrelian, B.; Parasyuk, O.; Ocheretova, V.; Khyzhun, O. Electronic structure and optical properties of $Ag_2HgSnSe_4$: First-principles DFT calculations and X-ray spectroscopy studies. *J. Alloys Compd.* **2018**, *732*, 372–384. [CrossRef]

43. Liu, B.-W.; Zhang, M.-J.; Zhao, Z.-Y.; Zeng, H.-Y.; Zheng, F.-K.; Guo, G.-C.; Huang, J.-S. Synthesis, structure, and optical properties of the quaternary diamond-like compounds I_2–II–IV–VI_4 (I = Cu; II = Mg; IV = Si, Ge; VI = S, Se). *J. Solid State Chem.* **2013**, *204*, 251–256. [CrossRef]

44. Hong, A.; Yuan, C.; Liu, J. Quaternary compounds Ag_2XYSe_4 (X = Ba, Sr; Y = Sn, Ge) as novel potential thermoelectric materials. *J. Phys. D Appl. Phys.* **2020**, *53*, 115302. [CrossRef]

45. Wang, C.; Ma, Q.; Xue, H.; Wang, Q.; Luo, P.; Yang, J.; Zhang, W.; Luo, J. Tetrahedral Distortion and Thermoelectric Performance of the Ag-Substituted $CuInTe_2$ Chalcopyrite Compound. *ACS Appl. Energy Mater.* **2020**, *3*, 11015–11023. [CrossRef]

46. Roychowdhury, S.; Ghosh, T.; Arora, R.; Samanta, M.; Xie, L.; Singh, N.K.; Soni, A.; He, J.; Waghmare, U.V.; Biswas, K. Enhanced atomic ordering leads to high thermoelectric performance in AgSbTe$_2$. *Science* **2021**, *371*, 722–727. [CrossRef]

47. Hong, M.; Chen, Z.G.; Yang, L.; Liao, Z.M.; Zou, Y.C.; Chen, Y.H.; Matsumura, S.; Zou, J. Achieving zT > 2 in p-Type AgSbTe$_{2-x}$Se$_x$ Alloys via Exploring the Extra Light Valence Band and Introducing Dense Stacking Faults. *Adv. Energy Mater.* **2018**, *8*, 1702333. [CrossRef]

48. Deng, S.; Jiang, X.; Zhang, Z.; Liu, J.; Chen, L.; Qi, N.; Tang, X.; Wu, Y.; Chen, Z. Structural features and thermoelectric performance of chalcopyrite Cu (In, Ga) Te$_2$ system by isoelectronic substitution. *Curr. Appl. Phys.* **2021**, *26*, 24–34. [CrossRef]

49. Zhong, Y.; Sarker, D.; Fan, T.; Xu, L.; Li, X.; Qin, G.Z.; Han, Z.K.; Cui, J. Computationally Guided Synthesis of High Performance Thermoelectric Materials: Defect Engineering in AgGaTe$_2$. *Adv. Electron. Mater.* **2021**, *7*, 2001262. [CrossRef]

50. Muchtar, A.R.; Srinivasan, B.; Tonquesse, S.L.; Singh, S.; Soelami, N.; Yuliarto, B.; Berthebaud, D.; Mori, T. Physical Insights on the Lattice Softening Driven Mid-Temperature Range Thermoelectrics of Ti/Zr-Inserted SnTe—An Outlook Beyond the Horizons of Conventional Phonon Scattering and Excavation of Heikes' Equation for Estimating Carrier Properties. *Adv. Energy Mater.* **2021**, *11*, 2101122. [CrossRef]

51. Barbier, T.; Srinivasan, B.; Berthebaud, D.; Eyert, V.; Frésard, R.; Macaigne, R.; Marinel, S.; Lebedev, O.I.; Guilmeau, E.; Maignan, A. Structural study and evaluation of thermoelectric properties of single-phase isocubanite (CuFe$_2$S$_3$) synthesized via an ultra-fast efficient microwave radiation technique. *Sustain. Energy Fuels* **2021**, *5*, 5804–5813. [CrossRef]

52. Azam, S.; Khan, S.A.; Minar, J.; Khan, W.; Din, H.U.; Khenata, R.; Murtaza, G.; Bin-Omran, S.; Goumri-Said, S. Coulomb interaction and spin-orbit coupling calculations of thermoelectric properties of the quaternary chalcogenides Tl$_2$PbXY$_4$ (X = Zr, Hf and Y = S, Se). *Semicond. Sci. Technol.* **2015**, *30*, 105018. [CrossRef]

53. Selezen, A.; Olekseyuk, I.; Myronchuk, G.; Smitiukh, O.; Piskach, L. Synthesis and structure of the new semiconductor compounds Tl$_2$B^{II}D^{IV}X$_4$ (B^{II}–Cd, Hg; D^{IV}–Si, Ge; X–Se, Te) and isothermal sections of the Tl$_2$Se–CdSe-Ge (Sn)Se$_2$ systems at 570 K. *J. Solid State Chem.* **2020**, *289*, 121422. [CrossRef]

54. Vu, T.V.; Lavrentyev, A.; Gabrelian, B.; Selezen, A.; Piskach, L.; Myronchuk, G.; Denysyuk, M.; Tkach, V.; Pham, K.D.; Khyzhun, O. Crystal growth, electronic and optical properties of Tl$_2$CdSnSe$_4$, a recently discovered prospective semiconductor for application in thin film solar cells and optoelectronics. *Opt. Mater.* **2021**, *111*, 110656. [CrossRef]

55. Mozolyuk, M.Y.; Piskach, L.; Fedorchuk, A.; Olekseyuk, I.; Parasyuk, O. Physico-chemical interaction in the Tl$_2$Se–HgSe–DIVSe$_2$ systems (DIV–Si, Sn). *Mater. Res. Bull.* **2012**, *47*, 3830–3834. [CrossRef]

56. Lavrentyev, A.; Gabrelian, B.; Vu, T.V.; Ananchenko, L.; Myronchuk, G.; Parasyuk, O.; Tkach, V.; Kopylova, K.; Khyzhun, O. Electronic and optical properties of quaternary sulfide Tl$_2$HgSnS$_4$, a promising optoelectronic semiconductor: A combined experimental and theoretical study. *Opt. Mater.* **2019**, *92*, 294–302. [CrossRef]

57. Bagci, S.; Yalcin, B.G.; Aliabad, H.R.; Duman, S.; Salmankurt, B. Structural, electronic, optical, vibrational and transport properties of CuBX$_2$ (X = S, Se, Te) chalcopyrites. *RSC Adv.* **2016**, *6*, 59527–59540. [CrossRef]

58. Cao, Y.; Su, X.; Meng, F.; Bailey, T.P.; Zhao, J.; Xie, H.; He, J.; Uher, C.; Tang, X. Origin of the Distinct Thermoelectric Transport Properties of Chalcopyrite ABTe$_2$ (A = Cu, Ag; B = Ga, In). *Adv. Funct. Mater.* **2020**, *30*, 2005861. [CrossRef]

59. Yang, J.; Fan, Q.; Cheng, X. Prediction for electronic, vibrational and thermoelectric properties of chalcopyrite AgX (X = In, Ga) Te$_2$: PBE+ U approach. *R. Soc. Open Sci.* **2017**, *4*, 170750. [CrossRef]

60. Qiu, P.; Qin, Y.; Zhang, Q.; Li, R.; Yang, J.; Song, Q.; Tang, Y.; Bai, S.; Shi, X.; Chen, L. Intrinsically High Thermoelectric Performance in AgInSe$_2$ n-Type Diamond-Like Compounds. *Adv. Sci.* **2018**, *5*, 1700727. [CrossRef]

61. Zhong, Y.; Luo, Y.; Li, X.; Cui, J. Silver vacancy concentration engineering leading to the ultralow lattice thermal conductivity and improved thermoelectric performance of Ag$_{1-x}$InTe$_2$. *Sci. Rep.* **2019**, *9*, 18879. [CrossRef] [PubMed]

62. Zou, D.; Xie, S.; Liu, Y.; Lin, J.; Li, J. First-principles study of thermoelectric and lattice vibrational properties of chalcopyrite CuGaTe$_2$. *J. Alloys Compd.* **2013**, *570*, 150–155. [CrossRef]

63. Ahmed, F.; Tsujii, N.; Mori, T. Microstructure analysis and thermoelectric properties of iron doped CuGaTe$_2$. *J. Mater.* **2018**, *4*, 221–227. [CrossRef]

64. Qin, Y.; Qiu, P.; Liu, R.; Li, Y.; Hao, F.; Zhang, T.; Ren, D.; Shi, X.; Chen, L. Optimized thermoelectric properties in pseudocubic diamond-like CuGaTe$_2$ compounds. *J. Mater. Chem. A* **2016**, *4*, 1277–1289. [CrossRef]

65. Yaseen, M.S.; Sun, J.; Fang, H.; Murtaza, G.; Sholl, D.S. First-principles study of electronic and optical properties of ternary compounds AuBX$_2$ (X = S, Se, Te) and AuMTe$_2$ (M = Al, In, Ga). *Solid State Sci.* **2021**, *111*, 106508. [CrossRef]

66. Dongho-Nguimdo, G.; Igumbor, E.; Zambou, S.; Joubert, D.P. First principles prediction of the solar cell efficiency of chalcopyrite materials AgMX$_2$ (M = In, Al; X = S, Se, Te). *Comput. Condens. Matter* **2019**, *21*, e00391. [CrossRef]

67. Wernick, J.; Geller, S.; Benson, K. Constitution of the AgSbSe$_2$$_-$AgSbTe$_2$–AgBiSe$_2$–AgBiTe$_2$ system. *J. Phys. Chem. Solids* **1958**, *7*, 240–248. [CrossRef]

68. Wu, H.-J.; Wei, P.-C.; Cheng, H.-Y.; Deng, J.-R.; Chen, Y.-Y. Ultralow thermal conductivity in n-type Ge-doped AgBiSe$_2$ thermoelectric materials. *Acta Mater.* **2017**, *141*, 217–229. [CrossRef]

69. Hoang, K.; Mahanti, S.; Salvador, J.R.; Kanatzidis, M.G. Atomic ordering and gap formation in Ag-Sb-based ternary chalcogenides. *Phys. Rev. Lett.* **2007**, *99*, 156403. [CrossRef]

70. Goto, Y.; Nishida, A.; Nishiate, H.; Murata, M.; Lee, C.; Miura, A.; Moriyoshi, C.; Kuroiwa, Y.; Mizuguchi, Y. Effect of Te substitution on crystal structure and transport properties of AgBiSe$_2$ thermoelectric material. *Dalton Trans.* **2018**, *47*, 2575–2580. [CrossRef]

71. Liu, X.-C.; Wang, Y.-M.; Qi, M.-L.; Pan, M.-Y. Enhanced thermoelectric properties in Ag-rich AgSbSe$_2$. *J. Solid State Chem.* **2020**, *288*, 121454. [CrossRef]

72. Wojciechowski, K.; Tobola, J.; Schmidt, M.; Zybala, R. Crystal structure, electronic and transport properties of AgSbSe$_2$ and AgSbTe$_2$. *J. Phys. Chem. Solids* **2008**, *69*, 2748–2755. [CrossRef]

73. Guin, S.N.; Chatterjee, A.; Negi, D.S.; Datta, R.; Biswas, K. High thermoelectric performance in tellurium free p-type AgSbSe$_2$. *Energy Environ. Sci.* **2013**, *6*, 2603–2608. [CrossRef]

74. Guin, S.N.; Chatterjee, A.; Biswas, K. Enhanced thermoelectric performance in p-type AgSbSe$_2$ by Cd-doping. *RSC Adv.* **2014**, *4*, 11811–11815. [CrossRef]

75. Li, D.; Qin, X.; Zou, T.; Zhang, J.; Ren, B.; Song, C.; Liu, Y.; Wang, L.; Xin, H.; Li, J. High thermoelectric properties for Sn-doped AgSbSe$_2$. *J. Alloys Compd.* **2015**, *635*, 87–91. [CrossRef]

76. Lee, J.K.; Oh, M.-W.; Ryu, B.; Lee, J.E.; Kim, B.-S.; Min, B.-K.; Joo, S.-J.; Lee, H.-W.; Park, S.-D. Enhanced thermoelectric properties of AgSbTe$_2$ obtained by controlling heterophases with Ce doping. *Sci. Rep.* **2017**, *7*, 4496. [CrossRef] [PubMed]

77. Ching, W.-Y.; Rulis, P. *Electronic Structure Methods for Complex Materials: The Orthogonalized Linear Combination of Atomic Orbitals*; Oxford University Press: Oxford, UK, 2012.

78. Giannozzi, P.; Baroni, S.; Bonini, N.; Calandra, M.; Car, R.; Cavazzoni, C.; Ceresoli, D.; Chiarotti, G.L.; Cococcioni, M.; Dabo, I. QUANTUM ESPRESSO: A modular and open-source software project for quantum simulations of materials. *J. Phys. Condens. Matter* **2009**, *21*, 395502. [CrossRef]

79. Hasan, S.; Adhikari, P.; Baral, K.; Ching, W.-Y. Conspicuous interatomic bonding in chalcogenide crystals and implications on electronic, optical, and elastic properties. *AIP Adv.* **2020**, *10*, 075216. [CrossRef]

80. Hasan, S.; Baral, K.; Li, N.; Ching, W.-Y. Structural and physical properties of 99 complex bulk chalcogenides crystals using first-principles calculations. *Sci. Rep.* **2021**, *11*, 9921. [CrossRef]

81. Kresse, G.; Furthmüller, J. Efficient iterative schemes for ab initio total-energy calculations using a plane-wave basis set. *Phys. Rev. B* **1996**, *54*, 11169. [CrossRef]

82. Dharmawardhana, C.; Bakare, M.; Misra, A.; Ching, W.Y. Nature of interatomic bonding in controlling the mechanical properties of calcium silicate hydrates. *J. Am. Ceram. Soc.* **2016**, *99*, 2120–2130. [CrossRef]

83. Adhikari, P.; Khaoulaf, R.; Ez-Zahraouy, H.; Ching, W.-Y. Complex interplay of interatomic bonding in a multi-component pyrophosphate crystal: K$_2$Mg (H$_2$P$_2$O$_7$)$_2$ H$_2$O. *R. Soc. Open Sci.* **2017**, *4*, 170982. [CrossRef]

84. Poudel, L.; Tamerler, C.; Misra, A.; Ching, W.-Y. Atomic-Scale Quantification of Interfacial Binding between Peptides and Inorganic Crystals: The Case of Calcium Carbonate Binding Peptide on Aragonite. *J. Phys. Chem. C* **2017**, *121*, 28354–28363. [CrossRef]

85. San, S.; Li, N.; Tao, Y.; Zhang, W.; Ching, W.Y. Understanding the atomic and electronic origin of mechanical property in thaumasite and ettringite mineral crystals. *J. Am. Ceram. Soc.* **2018**, *101*, 5177–5187. [CrossRef]

86. Hunca, B.; Dharmawardhana, C.; Sakidja, R.; Ching, W.-Y. Ab initio calculations of thermomechanical properties and electronic structure of vitreloy Zr$_{41.2}$Ti$_{13.8}$Cu$_{12.5}$Ni$_{10}$Be$_{22.5}$. *Phys. Rev. B* **2016**, *94*, 144207. [CrossRef]

87. Ching, W.Y.; Yoshiya, M.; Adhikari, P.; Rulis, P.; Ikuhara, Y.; Tanaka, I. First-principles study in an inter-granular glassy film model of silicon nitride. *J. Am. Ceram. Soc.* **2018**, *101*, 2673–2688. [CrossRef]

88. Ching, W.-Y.; Poudel, L.; San, S.; Baral, K. Interfacial interaction between suolunite crystal and silica binding peptide for novel bioinspired cement. *ACS Comb. Sci.* **2019**, *21*, 794–804. [CrossRef]

89. Poudel, L.; Twarock, R.; Steinmetz, N.F.; Podgornik, R.; Ching, W.-Y. Impact of Hydrogen Bonding in the Binding Site between Capsid Protein and MS$_2$ Bacteriophage ssRNA. *J. Phys. Chem. B* **2017**, *121*, 6321–6330. [CrossRef]

90. Adhikari, P.; Li, N.; Shin, M.; Steinmetz, N.F.; Twarock, R.; Podgornik, R.; Ching, W.-Y. Intra-and intermolecular atomic-scale interactions in the receptor binding domain of SARS-CoV-2 spike protein: Implication for ACE2 receptor binding. *Phys. Chem. Chem. Phys.* **2020**, *22*, 18272–18283. [CrossRef]

91. Mulliken, R.S. Electronic population analysis on LCAO–MO molecular wave functions. I. *J. Chem. Phys.* **1955**, *23*, 1833–1840. [CrossRef]

92. Dharmawardhana, C.; Misra, A.; Ching, W.-Y. Quantum mechanical metric for internal cohesion in cement crystals. *Sci. Rep.* **2014**, *4*, 7332. [CrossRef]

93. Giannozzi, P.; Andreussi, O.; Brumme, T.; Bunau, O.; Nardelli, M.B.; Calandra, M.; Car, R.; Cavazzoni, C.; Ceresoli, D.; Cococcioni, M. Advanced capabilities for materials modelling with Quantum ESPRESSO. *J. Phys. Condens. Matter* **2017**, *29*, 465901. [CrossRef] [PubMed]

94. Madsen, G.K.; Singh, D.J. BoltzTraP. A code for calculating band-structure dependent quantities. *Comput. Phys. Commun.* **2006**, *175*, 67–71. [CrossRef]

95. Ziman, J.M. *Electrons and Phonons: The Theory of Transport Phenomena in Solids*; Oxford University Press: Oxford, UK, 2001.

96. Allen, P.B.; Pickett, W.E.; Krakauer, H. Anisotropic normal-state transport properties predicted and analyzed for high-T$_c$ oxide superconductors. *Phys. Rev. B* **1988**, *37*, 7482. [CrossRef] [PubMed]

97. Singh, D.J.; Mazin, I. Calculated thermoelectric properties of La-filled skutterudites. *Phys. Rev. B* **1997**, *56*, R1650. [CrossRef]

98. Zhu, H.; Sun, W.; Armiento, R.; Lazic, P.; Ceder, G. Band structure engineering through orbital interaction for enhanced thermoelectric power factor. *Appl. Phys. Lett.* **2014**, *104*, 082107. [CrossRef]

99.   Zhu, H.; Hautier, G.; Aydemir, U.; Gibbs, Z.M.; Li, G.; Bajaj, S.; Pöhls, J.-H.; Broberg, D.; Chen, W.; Jain, A. Computational and experimental investigation of TmAgTe$_2$ and XYZ$_2$ compounds, a new group of thermoelectric materials identified by first-principles high-throughput screening. *J. Mater. Chem. C* **2015**, *3*, 10554–10565. [CrossRef]

100. Aydemir, U.; Pöhls, J.-H.; Zhu, H.; Hautier, G.; Bajaj, S.; Gibbs, Z.M.; Chen, W.; Li, G.; Ohno, S.; Broberg, D. YCuTe$_2$: A member of a new class of thermoelectric materials with CuTe$_4$-based layered structure. *J. Mater. Chem. A* **2016**, *4*, 2461–2472. [CrossRef]

101. Madsen, G.K.; Schwarz, K.; Blaha, P.; Singh, D.J. Electronic structure and transport in type-I and type-VIII clathrates containing strontium, barium, and europium. *Phys. Rev. B* **2003**, *68*, 125212. [CrossRef]

102. Bentien, A.; Pacheco, V.; Paschen, S.; Grin, Y.; Steglich, F. Transport properties of composition tuned α- and β-Eu$_8$Ga$_{16−x}$Ge$_{30+x}$. *Phys. Rev. B* **2005**, *71*, 165206. [CrossRef]

103. Pacheco, V.; Bentien, A.; Carrillo-Cabrera, W.; Paschen, S.; Steglich, F.; Grin, Y. Relationship between composition and charge carrier concentration in Eu$_8$Ga$_{16−x}$Ge$_{30+x}$ clathrates. *Phys. Rev. B* **2005**, *71*, 165205. [CrossRef]

104. Li, Y.; Ding, Y.; Xiao, B.; Cheng, Y. Anisotropic electrical and lattice transport properties of ordered quaternary phases Cr$_2$TiAlC$_2$ and Mo$_2$TiAlC$_2$: A first principles study. *Phys. Lett. A* **2016**, *380*, 3748–3755. [CrossRef]

105. Miyata, M.; Ozaki, T.; Takeuchi, T.; Nishino, S.; Inukai, M.; Koyano, M. High-throughput screening of sulfide thermoelectric materials using electron transport calculations with OpenMX and BoltzTraP. *J. Electron. Mater.* **2018**, *47*, 3254–3259. [CrossRef]

106. Madsen, G.K.; Carrete, J.; Verstraete, M.J. BoltzTraP$_2$, a program for interpolating band structures and calculating semi-classical transport coefficients. *Comput. Phys. Commun.* **2018**, *231*, 140–145. [CrossRef]

107. Cutler, M.; Leavy, J.; Fitzpatrick, R. Electronic transport in semimetallic cerium sulfide. *Phys. Rev.* **1964**, *133*, A1143. [CrossRef]

108. Snyder, G.J.; Toberer, E.S. Complex thermoelectric materials. In *Materials for Sustainable Energy: A Collection of Peer-Reviewed Research and Review Articles from Nature Publishing Group*; World Scientific: Singapore, 2011; pp. 101–110.

109. Gui, Y.; Ye, L.; Jin, C.; Zhang, J.; Wang, Y. The nature of the high thermoelectric properties of CuInX$_2$ (X = S, Se and Te): First-principles study. *Appl. Surf. Sci.* **2018**, *458*, 564–571. [CrossRef]

110. Kucek, V.; Drasar, C.; Navratil, J.; Plechacek, T.; Benes, L. Thermoelectric properties of Ni-doped CuInTe$_2$. *J. Phys. Chem. Solids* **2015**, *83*, 18–23. [CrossRef]

111. Xia, Z.; Wang, G.; Zhou, X.; Wen, W. Substitution defect enhancing thermoelectric properties in CuInTe$_2$. *Mater. Res. Bull.* **2018**, *101*, 184–189. [CrossRef]

112. Chen, H.; Yang, C.; Liu, H.; Zhang, G.; Wan, D.; Huang, F. Thermoelectric properties of CuInTe$_2$/graphene composites. *CrystEngComm* **2013**, *15*, 6648–6651. [CrossRef]

113. Kumar Gudelli, V.; Kanchana, V.; Vaitheeswaran, G.; Svane, A.; Christensen, N.E. Thermoelectric properties of chalcopyrite type CuGaTe$_2$ and chalcostibite CuSbS$_2$. *J. Appl. Phys.* **2013**, *114*, 223707. [CrossRef]

114. Plirdpring, T.; Kurosaki, K.; Kosuga, A.; Day, T.; Firdosy, S.; Ravi, V.; Snyder, G.J.; Harnwunggmoung, A.; Sugahara, T.; Ohishi, Y. Chalcopyrite CuGaTe$_2$: A high-efficiency bulk thermoelectric material. *Adv. Mater.* **2012**, *24*, 3622–3626. [CrossRef]

115. Yusufu, A.; Kurosaki, K.; Kosuga, A.; Sugahara, T.; Ohishi, Y.; Muta, H.; Yamanaka, S. Thermoelectric properties of Ag$_{1−x}$GaTe$_2$ with chalcopyrite structure. *Appl. Phys. Lett.* **2011**, *99*, 061902. [CrossRef]

116. Cai, S.; Liu, Z.; Sun, J.; Li, R.; Fei, W.; Sui, J. Enhancement of thermoelectric properties by Na doping in Te-free p-type AgSbSe$_2$. *Dalton Trans.* **2015**, *44*, 1046–1051. [CrossRef] [PubMed]

117. Hogarth, C. Applications of Thermo-Electricity. *Phys. Bull.* **1960**, *11*, 148. [CrossRef]

118. Gudelli, V.K.; Kanchana, V.; Vaithesswaran, G. CuAlTe$_2$: A promising bulk thermoelectric material. *J. Alloys Compd.* **2015**, *648*, 958–965. [CrossRef]

119. Dongho Nguimdo, G.; Joubert, D.P. A density functional (PBE, PBEsol, HSE06) study of the structural, electronic and optical properties of the ternary compounds AgAlX2 (X = S, Se, Te). *Eur. Phys. J. B* **2015**, *88*, 1–10. [CrossRef]

120. Asokamani, R.; Amirthakumari, R.; Rita, R.; Ravi, C. Electronic structure calculations and physical properties of ABX2 (A = Cu, Ag; B = Ga, In; X = S, Se, Te) ternary chalcopyrite systems. *Phys. Status Solidi (B)* **1999**, *213*, 349–363. [CrossRef]

121. Yaseen, M.S.; Murtaza, G.; Murtaza, G. Theoretical investigation of the structural stabilities, optoelectronic and thermoelectric properties of ternary alloys N a I n Y 2 (Y = S, S e and T e) through modified Becke–Johnson exchange potential. *Int. J. Mod. Phys. B* **2020**, *34*, 2050133. [CrossRef]

122. Aikebaier, Y.; Kurosaki, K.; Sugahara, T.; Ohishi, Y.; Muta, H.; Yamanaka, S. High-temperature thermoelectric properties of non-stoichiometric Ag1−xInTe2 with chalcopyrite structure. *Mater. Sci. Eng. B* **2012**, *177*, 999–1002. [CrossRef]